OFFICE OF NAVAL RESEARCH
DEPARTMENT OF THE NAVY
CONTRACT NONR-220(59)

WATER TUNNEL INVESTIGATIONS OF SCALE EFFECTS IN CAVITATION DETACHMENT FROM SMOOTH SLENDER BODIES AND CHARACTERISTICS OF FLOW PAST A BI-CONVEX HYDROFOIL

BY
VIJAY H. ARAKERI

DIVISION OF ENGINEERING AND APPLIED SCIENCE
CALIFORNIA INSTITUTE OF TECHNOLOGY
PASADENA, CALIFORNIA

REPORT NO. E-79A.12 JANUARY 1971

Engineering and Applied Science Division
California Institute of Technology
Pasadena, California 91109

WATER TUNNEL INVESTIGATIONS OF SCALE EFFECTS IN CAVITATION DETACHMENT FROM SMOOTH SLENDER BODIES AND CHARACTERISTICS OF FLOW PAST A BI - CONVEX HYDROFOIL

Office of Naval Research
Department of the Navy
Contract Nonr 220(59)

by

Vijay H. Arakeri

Report No. E-79A.12
January, 1971

Approved by:
A.J. Acosta

Acknowledgements.

The participation of all the members of the Hydrodynamics Laboratory staff, during the course of this experimental investigation is gratefully appreciated. In particular, the help of Messrs. H. Hamaguchi and C. Eastvedt is acknowledged. The author wishes to thank Dr. A. J. Acosta for his constant advice and encouragement at all times. The author also wishes to thank Dr. C. Brennen for helpful discussions. Thanks are due to Miss Cecilia Lin for the preparation of Figures and Mrs. Andy Van Scoyk for the typing.

NOMENCLATURE

c	=	Chord length of the hydrofoil
s	=	Span
ℓ	=	Cavity length
t_{max}	=	Maximum thickness of the hydrofoil
α	=	Angle of attack, degrees
A	=	Plan form area = $(sxc)ft^2$
ρ	=	Density of water, slugs/cu ft
V	=	Tunnel velocity, ft/sec
L	=	Lift force on model, lb
D	=	Drag force on model, lb
M	=	Moment on model, lb in
p_v	=	Vapor pressure of water, psi
p	=	Corrected tunnel static pressure, psi
σ	=	Cavitation number based on vapor pressure
	=	$(p - p_v) / \frac{1}{2} \rho V^2$
x	=	Distance from the leading edge of the cavitation detachment point on suction side at + ve angle of attack.
y	=	Distance from the leading edge to the cavitation detachment point on pressure side at + ve angle of attack
C_L	=	Lift coefficient = $L / \frac{1}{2} \rho V^2 A$
C_D	=	Drag coefficient = $D / \frac{1}{2} \rho V^2 A$
C_M	=	Moment coefficient = $M / \frac{1}{2} \rho V^2 Ac$ about the mid-chord point.
σ_i	=	Incipient cavitation number
Re_c	=	Reynolds number based on chord length
	=	Vc/ν

Re_{δ_2}	=	Reynolds number based on momentum thickness at the separation point
	=	$V \delta_2 / \nu$
γ	=	Air content in ppm (parts per million)

Abstract

Experimental results concerning force coefficients and cavity detachment points under various cavitating conditions on two geometrically similar bi-convex hydrofoils are presented. A linearized cavity flow theory with cavitation separation points determined from the assumption of smooth separation at the detachment point is presented and a comparison is made of these theoretical results with the experiments. Scaling problems with cavitation separation from smooth slender bodies are discussed. With the help of photographic studies three different types of cavitation separation from smooth bodies are proposed.

1. INTRODUCTION

In recent studies of cavitating flows past smooth bodies [1, 2]*, it was noticed that the cavitation detachment from spheres is subject to scale effects and the observed cavitation detachment points lie further downstream than predicted by theory using smooth separation at the detachment point. The purpose of present investigation is to look in to scaling problems associated with cavitation detachment and comparison of observed separation points with that obtained by assumption of smooth separation at the detachment points, for thin smooth hydrofoil sections, which are of practical importance. Two sharp edged, symmetric and geometrically similar bi-convex hydrofoil models with 6 in. and 3 in. chord lengths were chosen for experimental purposes. The simple geometry of this model made theoretical calculations much simpler than would have been for a model with blunt leading edge and sharp edged hydrofoils are of interest in themselves. The experimental results on force coefficients for the 3 in. model under cavitating and non-cavitating conditions and observed separation points for both the models are presented in main section of the report. A comparison of experimental and theoretical data is also made in the main section of the report. Linearized cavity flow analysis with arbitrary separation points past a sharp edged hydrofoil at an angle of attack is presented in appendix 1.

* Numbers in paranthesis refer to references at the end of the text.

2. EXPERIMENTAL PROCEDURE

The experiments described here were performed in the high speed water tunnel of the Hydrodynamics Laboratory at the California Institute of Technology. The working section of the tunnel is rectangular with the dimensions of 6 in. by 30 in. Two geometrically similar bi-convex hydrofoil models were tested whose dimensions and details are shown in figure (1). Both models are made of 416 stainless steel.

The models spanned the working section except for a small clearance at one of the ends; this clearance was set at a very low value of about 0.005 in. so that the gap effect was minimum on the forces. The models were mounted on a base plate which in turn was bolted to the spindle of the force balance so that the plate was set flush with the tunnel wall.

The forces on the 3 in. model (model 2) were measured by using the 3 component balance described in (3), the capacity of the balance limited the forces to be measured to 3.5° angle of attack at a free stream velocity of 40 ft/sec. Due to this same limitation no useful data on forces on the 6 in. model (model 1) could be obtained. Therefore most of the force measurements were carried out on the smaller 3 in. model. However some force measurements of the 6 in. model were made by measuring the deflection of the free end of the hydrofoil optically. These readings were converted to lift forces after calibrating the deflection of the model under known loads.

The force measurements were corrected for the balance interactions due to the change in tunnel static pressure and the tare forces on the mounting disk. The method of measuring tare forces is described in (4). In most cases the lift and moment corrections are negligible

whereas the tare drag force can be one third of the total drag force with fully wetted flow. Most of the tare drag force is due to the frictional forces on the mounting disk.

The location of pressure taps for the measurement of dynamic head and tunnel static pressure is shown in figure (2). The pressure measurements were made with mercury manometers. The dynamic head $(p_o - p_1)$ is used to calculate the free stream velocity V. To determine the effect of cavity length on tunnel static pressure measurements, additional pressures, p_2 and p_3, at two different upstream locations in the nozzle were measured. At low cavitation numbers, p_2 and p_3 differed up to a maximum value of 10 percent of p_1 for the 6 in. model. The difference at high cavitation numbers for the 6 in. model and at all cavitation numbers for the 3 in. model were very small. An average value of the two pressures was used to compute the free stream velocity and cavitation number σ.

The variation of σ was achieved by varying the tunnel static pressure p_2 to obtain the desired length of cavity, which could be observed through the lucite window, with fixed angle of attack α and free stream velocity. Still photographs of spanwise cavitation pattern were obtained for several cavitation numbers, angles of attack and velocities. With the help of these photographs cavitation separation points were estimated.

The air content of the water was measured on a Van Slyke blood gas analyzer. No special attempt was made to control the air content of the water in the tunnel.

The criterion for cavitation inception was based on visual observation of macroscopic sized bubbles in the minimum pressure area. Some attempts were made to study the flow characteristics over the hydrofoils under fully wetted conditions using oil film flow visualization techniques. This method and discussion of the observations are presented in appendix (II).

RESULTS

The non-cavitating lift and drag coefficients for the 3 in. model as a function of angle of attack at two different Reynolds number based on chord length are shown in fig. 3. Mid-chord pitching moment coefficient behavior with angle of attack at a Reynolds number of million is also shown in fig. 3. Figure 4 shows the behavior of lift and drag coefficients for the 3 in. model at a Reynolds number of 5×10^5 over a much wider range of angle of attack than shown in fig. 3. Behavior of lift coefficient for the 6 in. model at Reynolds number of 2×10^6 is also shown in fig. 4. Figure 5 shows the variation of drag coefficient as function of angle of attack and cavitation number. Similar results for lift and mid-chord pitching moment coefficients are shown in figs. 6 and 7 respectively. The range of cavitation number in figs. 5, 6 and 7 is such that to include conditions of fully wetted flow to fully cavitating flow. Figure 8 shows the variation of lift and drag coefficients

as function of angle of attack under fully cavitating conditions ($\sigma \sim .155$ - .095), fig. 8 also shows the theoretically obtained drag values based on linearized cavity flow theory developed in appendix (I). Figure 9 shows the variation of non-dimensional cavitation separation points for the two models tested, as function of cavitation number at zero angle of attack. The data shown in fig. 9 were obtained from still photographs taken at four different free stream velocities of 30, 40, 50 and 60 feet per second. Also shown are the theoretically obtained separation points from appendix (I). Figure 10 shows the cavitation inception data at zero angle of attack for the two models as function of free stream velocity. Figure 11 shows the comparison of inception data for the models used in present investigation with that of previous results for different hydrofoil models obtained from (5). Data on non-dimensional cavitation separation points for the two models on suction side and pressure side at different angles of attack and cavitation numbers is presented in Table 1, the theoretical data shown in Table 1 is obtained from appendix (I).

Figure 12 shows the behavior of lift coefficient as function of angle of attack under fully cavitating conditions for the following three different cases: 1) experimentally obtained lift coefficients, 2) theoretically obtained lift coefficients with the use of theoretically obtained cavitation separation points, 3) theoretically obtained lift coefficients with the use of experimentally measured cavitation separation points.

Similar calculations on drag coefficient are shown in fig. 8.

DISCUSSION OF RESULTS

A. NON-CAVITATING FLOW

Flow characteristics under fully wetted conditions are presented in figs. 3 and 4. Effect of Reynolds number is quite strong on the behavior of lift curve with angle of attack. The slopes of lift curves at Reynolds number of one million and two million is only $1.65\ \pi$, considerably below the expected value of 2π. At a Reynolds number of half a million, from fig. 4 it is evident that lift varies nonlinearly for small angles of attack up to 1.5°, then varies linearly up to an angle of attack of 6° with a slope of 2.06π and again varies nonlinearly up to the stall point which occurs at an angle of attack of 10°.

To understand this strange Reynolds number effect on the lift curve, oil film techniques for flow visualization were attempted as is discussed in appendix (II). From the observations presented in appendix (II), it is clear that there is a local laminar separation at the leading edge. Conditions near the trailing edge were not so well defined by this technique. The boundary layer was certainly thickened there as evidenced by the slow removal of the oil film especially on the suction side but no evidence of flow reversal was seen. Also it was not possible to ascertain the importance of the side wall boundary layers, although such three dimensional effects could be observed in the oil film. The best example of this is seen in fig. A2-2. The effect of Reynolds number on drag coefficients is less pronounced.

B. CAVITATING FLOW PHENOMENA

Establishment of cavitation on the models was done by the reduction of free stream pressure while the angle of attack and free stream velocity were held fixed. Therefore lowering of pressure means that cavitation number is also lowered.

Zero angle of attack : At this angle of attack beginning of cavitation took place on the models in the form of transient travelling macroscopic bubbles, and the cavitation numbers corresponding to this pressure is denoted as incipient cavitation number. From the explosive formation of these bubbles it is thought that the source of nuclei most probably comes from the free stream. As the cavitation number was reduced slightly (many times just due to fluctuation in free stream pressure) below the inception pressure, sudden formation of streaks of cavities was observed, these were photographed and are shown in figs. 21 and 22. The spanwise position of these macroscopic cavities were influenced by the presence of small disturbances at the leading edge, in some cases the disturbances were large enough to form a cavitating wake behind them. The eddies in the wake probably are good supply of nuclei. For all velocities tested further reduction in cavitation number for the 6 in. model resulted in growth of the streak like cavities in to larger sizes retaining a three dimensional pattern in the spanwise direction, an example of this is shown in fig. 15. Whereas for the 3 in. model except at velocity of 60 ft/sec., reduction in cavitation number produced dense population of macroscopic cavitation bubbles, which were uniformly distributed in the spanwise direction.

Further reduction of cavitation number did not change the structure of cavitation pattern. This difference in structure of macroscopic cavity probably produced observed difference in the lengths of cavities at the same cavitation number. One would imagine a much more efficient response in the cavity length due to pressure reduction in the case of streak type cavities than bubble type and this was consistently observed. At 60 ft. per sec. the cavitation observed on the 3 in. model was similar to that observed on 6 in. model. Further discussion on this point will be made later on in the report.

One degree angle of attack: Due to the sharp leading edge severe pressure gradients were experienced by the model on the suction side of the leading edge area. At high enough cavitation numbers a laminar separation bubble without cavitation was present to encounter the severe pressure gradients (see appendix II). As the cavitation number was decreased, first signs of cavitation appeared in the tip clearance area, further reduction in pressure produced a small cavitation bubble on the suction side of the leading edge. This cavitation bubble is comparable to the laminar separation bubble in the non-cavitating case, but the latter is usually accompanied by transition of boundary layer on the separated bubble, whereas no such indications were noticed on the separated cavitation bubble. Further reduction in pressure increased the leading edge bubble size and in many instances this was accompanied by high level auditory noise, it seemed as if the model was singing. Further reduction in pressure produced first signs of cavitation in the minimum pressure area. This type of

cavitation inception was quite different from the inception observed at zero angle of attack. This type of inception occurred with a formation of cavitating patch which was frothy in nature and similar to cavitation observed in wakes. An example of this is shown in fig.23. Further reduction in pressure diminished the size of leading edge bubble, but increased the cavitating area downstream of minimum pressure point in to the wake area. Finally at very small cavitation number the structure is exhibited in fig.16. In the same fig. 16, one can also notice the cavitating wake behind a large leading edge disturbance. It should be mentioned that no noticeable difference in cavitation pattern on the suction side, for the two models was observed.

Only at low cavitation numbers when large area of the suction side of model was cavitating, cavitation appeared on the pressure side of the models. On the 6 in. model the cavitation was in the form of streaks coming off the intersection of tunnel walls with the model and the pressure taps, which is illustrated in fig.28. These streaks of cavities were accompanied by the presence of large cavitation bubbles traveling in the free stream adjacent to the model surface. On the 3 in. model, at first the cavities were in the form of streaks adjacent to the intersection of tunnel walls and the model, but as the pressure was reduced cavities formed due to coalescence of large cavitation bubbles fixed to the surface of the model. At this point still large portion of the model surface was non-cavitating, only after further reduction in pressure did a suddent cavitating patch form, it was a fully developed cavitation patch with smooth glassy surface at the separation line. This type of cavitation has been observed on

axisymmetric bodies and is illustrated in fig. 29, which is taken from work reported in (12). Further reduction in cavitation number did not change the spanwise pattern only the streamwise lengths of the cavities increased. An illustration of above discussion is shown in fig. 26.

Two degree angle of attack: At 2^{o} angle of attack cavitation began with the formation of cavitation sheet (or bubble) on the suction side of the leading edge as was the case in 1^{o} case. Reduction of cavitation number increased the bubble size, and contrary to the 1^{o} case no inception of cavitation took place in the min. pressure area. Successive reduction of pressure just increased the size of the cavitation bubble, which had a smooth glassy surface except at the trailing edge. This smooth glassy surface appears as extremely dark portion on photographs. In this mode of cavitation the bubble size was extremely sensitive to slight changes in cavitation number. As soon as the cavity length reached .75 chord length an inherently unsteady mode developed and the cavity started oscillating in a cyclic manner, first the cavity would lift itself and then collapse violently on the model producing large amplitude vibrations of the model. A detailed study on this phenomena is reported in (6). Slight pressure changes did not effect the cavity length appreciably, only the amplitude of vibration of the model became smaller. After a large reduction in cavitation number the oscillations stopped and steady state cavity developed, whose appearance was similar to cavitation at 1^{o} angle of attack with low cavitation number. The leading edge bubble in this case was quite large and another large cavity starting slightly downstream of the trailing edge of the leading edge cavity was present. Therefore a fully wetted portion on the foil surface appeared

in the min. pressure area which was not present at a higher cavitation number, when the cavity length was about .75 chord length, this change is clearly illustrated in figs. (19) and (17). As will be pointed out later these shifts in cavitation pattern had pronounced effects on the forces encountered by the model. The suction side cavitation development for the two models was very similar in nature.

The cavitation pattern on the pressure side of 6 in. model at 2^{o} angle of attack was very similar in nature to that observed at 1^{o} angle of attack discussed earlier. Whereas on the 3 in. model a fairly uniform cavity in the spanwise direction was formed, the surface of the cavity at the detachment was glassy and clear indication of transition of the boundary layer on the cavity surface was present. This cavity is similar in nature to that observed on axisymmetric bodies (12), mentioned earlier and is shown in fig. (29). A regular spanwise destortion of the separation line is seen from the photograph in fig. (27), similar destortions are visible in the trailing portions of the leading edge cavitation bubble in fig. (17). Since the boundary layer characteristics for the two cases are quite different, the common real fluid effect of surface tension is thought to be responsible for the local destortions in the separation line seen in fig. (27).

For higher angles of attack the suction side cavitation development was similar in nature to that observed on a plano-convex hydrofoil and discussed in (6). Three distinct modes of cavitation were present and each is outlined separately in following paragraphs.

1. Partially Cavitating Zone: The inception of cavitation took place on the suction side of the leading edge in the form of a cavitation sheet

attached to the leading edge. The length of the bubble was extremely sensitive to reductions in pressure or cavitation number. Reduction in cavitation number increased the bubble size until the length of the cavity was about .75 chord length, then a new mode developed. Since the cavity length is less than chord length this zone is commonly known as partially cavitating zone.

2. Unsteady zone: As mentioned in previous paragraph as soon as the cavity length was about .75 chord length an unsteady zone developed, the cavity would lift itself up with leading edge as the hinge point and immediately collapse violently on the model producing violent oscillations of the model which were visible to the naked eye. A photograph of such a collapse is shown in fig. (20). It is apparent that energy exchange takes place between the free stream kinetic energy and the work done in expanding the cavitation bubble, but the mechanism of this exchange is as yet unclear. It should be concluded that expansion of cavity is not possible if the surrounding liquid is homogeneous and the tunnel walls are rigid. The whole process mentioned above was periodic and subsided after large reduction in the cavitation number and when the cavity length was about 1.1 chord lengths. The length of cavity in this zone was insensitive to slight pressure or cavitation number variations.

3. Fully Cavitating Zone: As soon as the cavity length reached about 1.1 chord lengths steady state returned and the cavity length was sensitive to slight cavitation number variations. In principle one can obtain an infinitely long cavity but in practice choking phenomena takes place, where the cavity length does not change as the cavitation number is decreased, commonly this is referred to as supercavitating zone. A photograph of the cavitation pattern at low cavitation number is shown

in fig. 18. For the present models choking took place when the cavity length was about 7-8 chord lengths.

It is clear from the above discussions that for practical purposes it would be advantageous to work either in a non-cavitating or fully cavitating zone. Even though a partially cavitating region is steady in nature, it is susceptible to unsteadiness with slight variations in free stream velocity or pressure. From material damage point of view also; a fully cavitating zone would be preferable to partially cavitating zone, since in the latter case the cavity ends on the material surface.

At higher angles of attack the cavitation pattern on the pressure side was highly non-uniform in the spanwise direction as observed in the case of 6 in. model at 1^{o} and 2^{o} angle of attack. Similar pattern was also observed on the 3 in. model.

To summarize partly the results a schematic sketch of change of cavitation pattern with angle of attack and cavitation numbers is shown in figs. 13 and 14.

C. SCALE EFFECTS IN CAVITATION INCEPTION. Cavitation inception data for the two models at zero angle of attack for various velocities is presented in fig. 10. Exact value of the C_p minimum neglecting viscous effects is also shown in the same fig. 10. Estimation of blockage effect was found to be less than 4 per cent of C_p min. value and therefore can safely be neglected.

As seen in fig. 10, the inception values for both models are higher than C_p min. at low velocities. Calculations with the help of air content measurements shown in fig. 10 indicate that at these low velocities air content is about 10 times the saturation value at 1 atmosphere. Therefore

it is possible that the observed cavitation is gaseous rather than vaporous. Another explanation for inception value being larger than C_p min. is that due to effects of surface protrusions or turbulence. Photographs taken at the inception conditions indicated that on the 6 in. model, no surface irregularities were responsible for premature cavitation but most probably the observed cavitation was gaseous. The position of inception was in the adverse pressure gradient area further downstream than min. pressure point. On the contrary from fig. 30 it is obvious that on the 3 in. model the leading edge disturbances are responsible for premature cavitation. The argument is supported further from the position of inception which is upstream of minimum pressure point. Values of desinence cavitation number higher than C_p min. have been reported previously by Holl (13), and his conclusion was that of observed cavitation being that of gaseous type. Present investigations indicate the importance of having photographs of inception conditions along with the pertinent data.

At this point it should be mentioned that initial inception in many instances was in the form of transient travelling macroscopic bubbles, which could not be photographed, but steady state inception took place with a very slight reduction in free stream pressure and these were photographed.

At higher velocities the inception values for 6 in. model were almost equal to C_p min. value or slightly above it, whereas for the 3 in. model they were always lower than C_p min. value. Photographic studies indicate that at these velocities leading edge disturbances played an important role in the inception process for the 6 in. model, whereas for the 3 in. model they were not apparent as they were for the case of 30 ft. per sec. in fig. 30. The leading edge disturbances were in the

form of either small debri sticking at the leading edge or local cavitation bubble formation due to the sharpness of the leading edge. These arguments are supported from inspection of photographs in figs.(21) and (22). It should be mentioned that the position of inception for the 3 in. model was further downstream than that for 6 in. model, but both were ahead of minimum pressure point.

The role of leading edge protrusions is to effect the status of boundary layer downstream of the disturbances (see appendix II and fig. A2-3), cause local pressure reduction and finally if the disturbances are large enough cause cavitating wakes, thus acting as good source of nuclei. It is also important to consider the status of flow after the disturbances, if the flow is subjected to severe favorable pressure gradients, then the effects would tend to be supressed or minimized and; if the flow is subjected to distributed roughness then the effects due to isolated roughness elements would tend to be distributed uniformly thus minimize the overall effectiveness of isolated disturbances. In this sense it is worthwhile to point out that smaller model was twice as rough as the larger model. The author does not believe that the roughness elements are the sole cause for the observed behavior in fig. 10.

The change in appearance of cavitation inception with velocity is shown in figs. (22), (31) and (32) for the 3 in. model. The form of inception at 40 ft. per sec. was in the form of isolated bubbles densely populated and fairly uniformly distributed in the spanwise direction and is shown in fig.(22). Whereas at 60 ft. per sec. as seen in fig.(32), small streaks of cavities were formed but small isolated bubbles existed

just prior to the beginning of the streaks. At 50 ft. per sec. the inception was in the form of isolated bubbles which were much larger in size than 40 ft. per sec. case and simultaneously some streaks of cavities were also present, this is illustrated in fig.(31). The appearance of cavitation inception for the 6 in. model was that of streak type for all the velocities as seen partly in figs. (21) and (33). This difference in appearance for the 3 in. model is probably reflected in the variation of σ_i with velocity. The inception values for 6 in. model did not vary appreciably with velocity for velocities higher than 40 ft. per sec. Similar behavior of inception values with velocity is reported in (14) for the case of cavitation in turbulent boundary layer on a smooth wall.

A different form of inception on the suction side of 6 in. model at 1^o angle of attack is shown in fig.(23). The cavitation is extremely frothy in nature, the inception cavitation number was found to be exactly equal to $C_p$min. value at 1^o angle of attack.

Figure 11 shows the averaged out inception data for three different hydrofoil sections. The data on NACA 16012 models and 12 percent Joukowski models are taken from (5). The behavior of inception data with Reynolds number and model size for the present models and NACA 16012 models is very similar, the only difference being that the inception values for the present models were close to theoretical $C_p$min. of .225, whereas the NACA16012 data was always way above the theoretical $C_p$min. of .293. The behavior of inception data for the 12 percent Joukowski models with model size and Reynolds number is in opposite trend from that observed for the present bi-convex models and NACA 16012 models. It should be noted that pressure distributions for the

bi-convex model and NACA 16012 model are very similar in nature being that of a flat type, whereas the pressure distribution for the 12 per cent Joukowski is that of a peaked type. Since the inception values for the NACA 16012 hydrofoils fell above the C_p min. value, it is felt that the observed cavitation was gaseous. If that is the case, then from present experiments it can be tentatively concluded that the effect of size and velocity on inception values does not depend on whether the cavitation is gaseous or vaporous. Since details of cavitation inception process on Joukowski hydrofoils are lacking, it is difficult to conclude about the drastic difference observed in the behavior of inception data shown in fig. 11. It is possible that the inception on Joukowski hydrofoils took under the conditions of laminar boundary layer whereas the present inception data is under turbulent boundary layer conditions.

D. SCALE EFFECTS IN CAVITATION DETACHMENT. From the discussion in Section VI-B on cavitating flow phenomena, it is apparent that many different types of cavitation detachment from the present hydrofoil sections were observed. The discussion carried on this section is focused on fully cavitating flows, where localized effects can be neglected in determining the cavitation detachment points and also theory developed in Appendix I is valid only for cavities with length greater than chord. It is postulated that the following three basically different types of cavitation separation are possible; namely,

1. Viscous laminar cavitation separation
2. Viscous turbulent cavitation separation
3. Nucleate cavitation separation

The first two types may be likened to conventional boundary layer separation in non-cavitating flow, since at the cavitation detachment point the conditions of viscous boundary layer separation would be met. Thus such separations are possible only in the presence of finite adverse pressure gradients such that the condition of wall shear stress going to zero is satisfied at the detachment point. The third type of separation is unique to cavitating flows only. It can occur in favorable pressure gradient area or in fact without the presence of boundary layer at all, but this does not mean that viscous effects do not influence the nucleate separation in real cavity flows. Good illustrations of the first type of separation are shown in figs. 27 and 29. This type of separation is accompanied by smooth glassy cavity at the separation line, spanwise distortion of the separation which is thought to be due to local effects of surface tension as discussed earlier in Section VI-B and transition of boundary layer to turbulence on the cavity surface slightly after the separation line. In (2) further examples of this type of separation are illustrated with the conclusion that this type of separation is mainly dependent on cavitation number and Reynolds number.

Examples of nucleate type of separation are shown in figs. 15, 16, 24 and 25. It is evident from the photographs that two distinct types of nucleate separation are present which could be called bubble type nucleate separation and streak type nucleate separation. During bubble type of separation the cavity formed is characterized by the presence of dense population of macroscopic cavitation bubbles. The separation point in this case is somewhat arbitrary in nature. An example of separation point used for the present purposes is shown by a dotted black line on fig. 24. Figures 16 and 24 are examples of this type of separation. During streak

type of separation the cavity formed is characterized by the presence of long finger-like cavities. The cavity has a three-dimensional character and a spanwise instability is present. The position of the finger-like cavities seems to be determined by the presence of small leading edge disturbances. Examples of this type of separation are shown in fig. 15 and 25.

At zero angle of attack except at velocity of 60 ft/sec the type of separation on the 3 in. model was that of bubble type nucleate separation, whereas for all velocities the type of separation for the 6 in. model was streak type nucleate separation. The type of separation for the 3 in. model switched from bubble type to streak type as the velocity was raised from 50 ft/sec to 60 ft/sec, which is clearly shown in figs. 24 and 25. This difference in type of separation for the two models is reflected in the observed data for the 3 in. model being always further downstream than the observed data for the 6 in. model, which is shown in fig. 9. The theoretical values shown in fig. 9 are obtained from Appendix I. It should be observed that detachment points measured for both the models fall further downstream than predicted by the linearized theory.

Fig. 35 shows a replot of fig. 10 with horizontal axis being Reynold's number based on momentum thickness at the separation point. The calculations shown in fig. 35 are based on approximating the forward portion of the model as a wedge of angle 9.5°. The quantities next to data points are corresponding cavitation numbers. The flagged quantities are points with nucleate streak separation and unflagged quantities are with nucleate bubble type separation. It is conjectured that the critical Reynolds number in distinguishing the two types is about 350. Author feels that the transition process which occurs at critical Reynolds number of about 400 is influential in determining the type of separation.

As seen from fig. 35, it is apparent that for a fixed size as the velocity is decreased viscous effects on separation become stronger. Similar effects are seen as the size is reduced for a fixed velocity. Also shown on the figure are separation points (dotted lines) from linearized theory (Appendix I) at the corresponding cavitation numbers marked on the dotted lines. The comparison between the theoretical and experimental results shows that the agreement improves as the Reynolds number increases.

The still difficult question to be answered is when to expect what kind of cavitation separation. To answer this question it is assumed that the favorable pressures for the growth of cavitation bubbles have reached at the theoretically predicted detachment point (Th.C.S.P.) and that the laminar (L.C.S.P.) and turbulent (T.C.S.P.) cavitation separation points are in the neighborhood of conventionally estimated laminar and turbulent boundary layer separation points. It should be realized that this will not be the case in reality due to the effect on pressure distribution; on the model surface; due to cavitation in surrounding flow areas. For example in the case of present models at angle of attack, cavitation separation on the pressure side would be influenced by the presence of cavitation on the suction side. Now if the flow is laminar and conditions for cavitation nuclei to grow to macroscopic size are favorable between Th.C.S.P. and L.C.S.P., then the cavitation separation will be that of nucleate type—otherwise it will be that of viscous laminar type. If transition of boundary layer takes place before laminar separation point is reached and conditions for cavitation nuclei to grow to macroscopic size are favorable between Th.C.S.P. and T.C.S.P., then the cavitation separation will be again that of nucleate type. Favorable conditions for the growth of cavitation nuclei to macroscopic size are

that, abundant supply of nuclei should exist and the residence time of these nuclei in low pressure area should be long enough for the growth to occur. It should be noted that chances of these conditions being met are much higher for the case, where, transition takes place before laminar separation point and thus enhancing the chances of having a nucleate separation. Therefore it may be said that bluff bodies like spheres and cylinders would tend to have laminar cavitation separation, whereas bodies with long slender shapes like present models would tend to have nucleate type separation. Conditions of two different types of separation occurring simultaneously are also possible.

At angle of attack the observed separation points on the suction side were influenced by the presence of leading edge cavitation bubble and on the pressure side; separation was influenced by the cavities springing off the tunnel walls. The meager data obtained is shown in Table 1. The observed separation on suction side was that of nucleate bubble type and an example of this is shown in fig. 16. For all angles of attack the separation on the pressure side of the 6 in model was not regular in nature, a representative example of separation observed is shown in fig.28. The only cavities present are off the pressure taps and tunnel walls. Separation on pressure side for the 3 in. model at an angle of attack of 1^{o} is shown in fig.26, portions of foil surface has nucleate bubble type and portions have viscous laminar type. Separation on pressure side for the 3 in. model at an angle of attack of 2^{o} is shown in fig.27, the separation is that of viscous laminar type. The separation observed on pressure side for the 3 in. model at higher angles of attack was similar to the separation observed on 6 in. model as shown in fig.28. The theoretical data

shown in Table 1 is taken from appendix 1. Discrepancy between the theory and experiment on the pressure side is quite high.

A clear example of viscous turbulent separation was not observed in present experiments and therefore is not discussed in great detail.

E. FORCES IN CAVITATING FLOW: Force coefficients for the 3 in. model as function of cavitation number and angle of attack are shown in figs. 5, 6 and 7. As mentioned previously the range of cavitation number covers three distinct cavitating flow regimes and a discussion on behavior of force coefficients in these regions is done separately for convenience sake.

1) Partially Cavitating Zone: ($\sigma \sim .4 - .8$). The length of cavity in this zone is less than .75 chord length. For angles greater than 1^{o}. The presence of leading edge cavitation bubble whose length increases as cavitation number is decreased results in the reduction of skin friction on the model and this is reflected in the reduction of drag values as cavitation number is decreased. This behavior on drag coefficient is shown in fig. 5. At the same time the increase in the size of leading edge bubble adds increasing amount of camber to the otherwise symmetric profile, thus resulting in increase of lift coefficient with increase in bubble size or decrease in cavitation number. Increase in lift values produce higher moments, and this behavior on lift and moment coefficients is shown in figs. 6 and 7.

2) Unsteady Zone: ($\sigma \sim .2 - .4$) The length of cavity in this zone is between .75 and 1.1 chord lengths. This zone is characterized by

oscillating unsteady forces and the data obtained with the 3 component balance is very unreliable, for a detailed look at this phenomena see (6). This region is shown by dotted lines in figs. 5, 6 and 7.

3) Fully Cavitating Zone: ($\sigma \sim .05 - .2$) The length of cavity in this zone is greater than 1.1 chord lengths. The drag values except at angles of 0^{o}, $.5^{o}$ and 2^{o} decrease as cavitation number is decreased. This same behavior is noticed at all angles for theoretically obtained drag coefficients and is shown in fig. A1.6 (appendixI).

A comparison of theoretically obtained drag values from appendix I and experimental drag values for small cavitation numbers ($\sigma \sim .155 - .095$) is shown in fig. 8. Except at 2^{o} the agreement is quite good. The lift coefficients found in this region are considerably smaller than the ones observed in partially cavitating zone, in fact the lift values are negative for positive angles of attack for low cavitation numbers. This interesting behavior of lift coefficient with angle of attack at low cavitation numbers ($\sigma \sim .155 - .095$) is shown in fig. 8. A comparison of theoretical lift coefficients with the use of separation points determined from smooth separation conditions (appendix I), theoretical lift coefficients with the use of observed separation points (appendix I) and experimentally obtained lift coefficients is made in fig. 12. These differences are attributed to the discrepancies observed in separation points on the pressure side of the hydrofoil as shown in Table 1. With the help of the theoretical data and observed cavitation pattern from photographs, possible pressure distribution on the suction and pressure sides of the hydrofoil are shown in fig. 34. It was assumed that vapor pressure value is reached at the theoretical separation point. A careful study of the diagrams in fig. 34 should provide justification for the observed trend of lift coefficients with angle of attack and

negative lift coefficients at positive angles of attack. Therefore the main reason for the presence of negative lift is the delay in cavitation separation on the pressure side due to the viscous effects mentioned before. One must conclude that the delay in separation causes large areas of the hydrofoil on the pressure side to be in a state of tensions or at least with pressures less than the vapor pressure. An approximate bound on tensions possible is -8cm-Hg (15).

As seen in fig. 12, when the observed separation points were used to calculate the theoretical lift coefficients, the agreement is quite good for angles of attack of 1^{o} and 2^{o}, where observed flow is almost 2-dimensional as assumed in theory. At an angle of attack of 3^{o} the pressure side separation point used in the calculation was at the trailing edge, but as seen from fig. 28, the actual flow is highly three dimensional whose account is not taken into a 2-D theory and thus resulting in much higher observed lift value than predicted by theory.

Similar calcuations in the case of drag values are shown in fig. 8. The agreement between experimental drag values and theoretically obtained drag values is quite good at 0^{o} angle of attack. But at other angles of attack the smooth separation drag values have better agreement with experimental values than drag values calculated from use of observed separation points.

As discussed previously and illustrated in fig. 14 a unique shift in cavitation pattern took place for the case of 2^{o} angle of attack, and this behavior is reflected in the unique behavior of drag coefficient

with cavitation number in fig. 5 for the case of angle of attack of 2^{o}.

Since the moments are based on mid-chord point, positive moments are possible even though the corresponding lift values are negative, this was observed in present experiments and is shown in fig. 7.

F. ON THE MODELING OF CAVITATION SEPARATION WITH SMOOTH SEPARATION CONDITION: In linearized cavity flow analysis (potential flow) past smooth bodies, the determination of separation points is done by the application of smooth separation condition at the cavity detachment point, which physically means that, flow should leave the solid body tangentially at the detachment point. A mathematical statement of this condition is given in Appendix I. From present experimental results and others (1, 2) it is evident that the predicted separation points differed considerably from observed separation points in the case of viscous laminar type separation and to a lesser extent in the case of nucleate type. From fig. 9, in the case of nucleate type of separation it is indicative that at high Reynolds number, and low cavitation numbers the agreement is quite adequate. In the work of C. Brennen (1) it was found that for bluff bodies like spheres the modeling of flow is quite adequate, even though the predicted separation point was found to be upstream than observed separation point. The observed separation on the spheres was that of viscous laminar type. This descrepancy in prediction of separation point resulted in poor agreement between predicted and observed lift values as shown in fig. 12, at the same time the agreement for drag values was quite good as shown in fig. 8.

5. SUMMARY AND CONCLUSIONS

1) It was found that the lift coefficient of sharp edged hydrofoils under non-cavitating conditions is subject to a strong Reynold's number effect.

2) Under cavitating conditions the following three types of cavitation detachment are proposed for the type of hydrofoil studied:

i) Viscous laminar cavitation separation

ii) Viscous turbulent cavitation separation

iii) Nucleate cavitation separation

Nucleate separation is further subdivided into a "bubble type" and a "streak type" of separation. The form of the nucleate separation is dependent on cavitation number and Reynold's number based on momentum thickness at the separation point.

3) Cavitation inception data are subject to scale effects with size and velocity. For the present models the inception values decreased with decreasing model size and increasing velocities. The size effect is believed to be due to leading edge disturbances due to microscopic debris in the tunnel flow impinging upon the leading edge of the hydrofoil.

4) The observed separation positions were always further downstream than separation points calculated from free streamline theory. At zero angle of attack the agreement improved with increase in Reynold's number. Viscous effects played an important role in determining the site of the cavitation detachment points. The observed values were 10 percent further downstream for the nucleate streak separation, 50 percent for the nucleate bubble separation, and 100 percent for the viscous laminar separation.

5) Cavitation detachment from smooth bodies is subject to pronounced scale effects, especially with size and velocity. At zero angle of attack, the position of separation was further downstream as model size was decreased. A better correlation was obtained when a plot of Reynold's number based on momentum thickness at the separation point vs. non-dimensional cavity detachment point was made.

6) The delay in separation on the pressure side of the hydrofoil at an angle of attack due to viscous effects resulted in negative lift coefficients at small positive angles of attack.

7) In most cases, it was observed that for smooth separation - as opposed to separation from the leading edge, the cavity detachment process was highly non two-dimensional.

8) Linearized cavity flow theory predicts lift values very poorly on these smooth bodies. The predicted values have positive signs at 1^{o}, 2^{o}, and 3^{o} angle of attack, whereas the observed lift coefficients are negative for the same angles of attack. When the observed separation points were used in the theory to predict the force coefficients the agreement was better; the lift forces were reasonably estimated then but the drag forces estimated worse.

REFERENCES

1. Brennen, C., "A Numerical Solution of Axisymmetric Cavity Flows", J. Fluid Mech. (1969), Vol. 37, part 4, pp. 671-688.

2. Brennen, C., "Some Viscous and Other Real Fluid Effects in Fully Developed Cavity Flows", Symposium on Cavitation State of Knowledge, published by the A.S.M.E., 345 East 47th Street, New York, N.Y. 10017.

3. Hotz, G.M.; McGraw, J.T., "The High Speed Water Tunnel Three-Component-Force Balance", California Institute of Technology, Hydrodynamics Laboratory, Report No. 47-2 (1955).

4. Kermeen, R.N., "Water Tunnel Tests of N.A.C.A. 4412 and Walchner Profile 7 Hydrofoils in Non-Cavitating and Cavitating Flows", California Institute of Technology, Hydrodynamics Laboratory, Report No. 47-5 (1956).

5. Holl, J.W.; Wislicenus, G.F., "Scale Effects on Cavitation", Journal of Basic Engineering, Trans. A.S.M.E., Series D, Vol. 83, 1961, pp. 385-398.

6. Wade, R.B.; Acosta, A.J., "Experimental Observations on the Flow Past a Plano-Convex Hydrofoil", Trans. A.S.M.E., Journal of Basic Engineering, Paper Presented June 7, 1965, Applied Mechanics/Fluids Engineering Conference, Washington, D.C..

7. Birkhoff, G., (1950) Hydrodynamics. Princeton University Press.

8. Muskhelishvili, N.I., "Singular Integral Equations", P. Noordhoff, Limited, Goningen, Netherlands, 1946.

9. Parkin, B.R., "Linearized Theory of Cavity Flow In Two Dimensions", Rand Corporation Report P-1745, 1959.

10. Wu, T. Yao-Tsu, Unpublished work.

11. Wu, T. Yao-Tsu, "A Note on the Linear and Nonlinear Theories for Fully Cavitated Hydrofoils", Hydrodynamics Laboratory, California Institute of Technology, Report No. 21-22, 1956.

12. Acosta, A.J., Hamaguchi, H., "Cavitation Inception on the I.T.T.C. Standard Head Form", Report No. E-149.1 Hydrodynamics Laboratory, California Institute of Technology, March, 1967.

13. Holl, J.W., "An Effect of Air Content on the Occurence of Cavitation", Journal of Basic Engineering, Trans. A.S.M.E., Series D, Vol. 82, pp. 941-946.

14. Arndt, R.E.A., Daily, J.W., "Cavitation in Turbulent Boundary Layers", Symposium on Cavitation State of Knowledge, published by the A.S.M.E., 345 East 47th Street, New York, N.Y..

15. Parkin, B.R., Kermeen, R.W., "The Roles of Convective Air Diffusion and Liquid Tensile Stresses During Cavitation Inception", Proceedings of I.A.H.R., Symposium on Cavitation and Hydraulic Machinery, Institute of High Speed Mechanics, Tohoku University, Sendai, Japan, 1962.

16. Schlichting, H., "Boundary-Layer Theory", McGraw Hill, 1968.

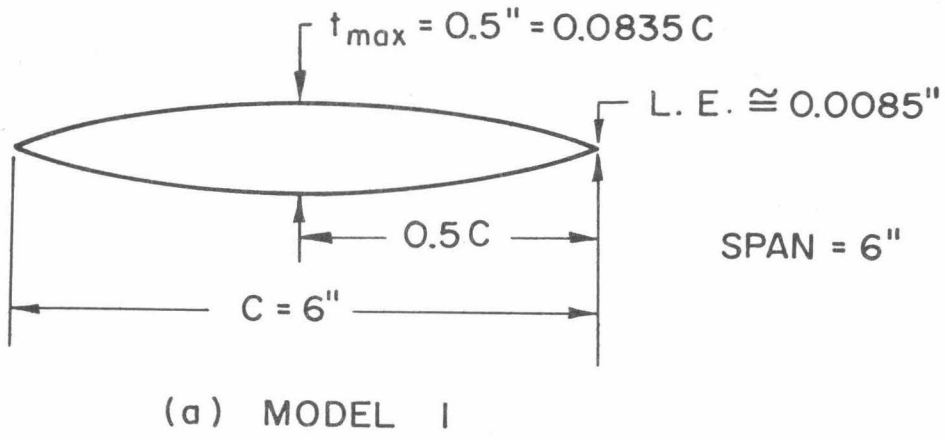

(a) MODEL 1

Figure 1(a), (b) Geometry of 6 inch and 3 inch models with average surface roughness of 20 and 35 microinches respectively.

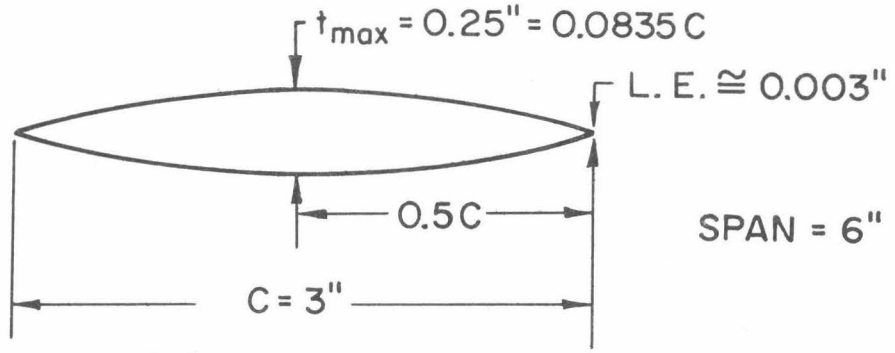

(b) MODEL 2

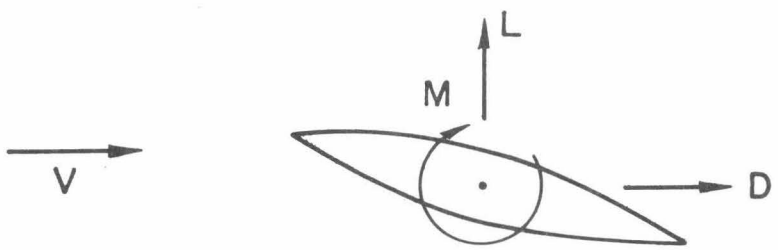

(c)

Figure 1(c) Positive sense of forces and moment.

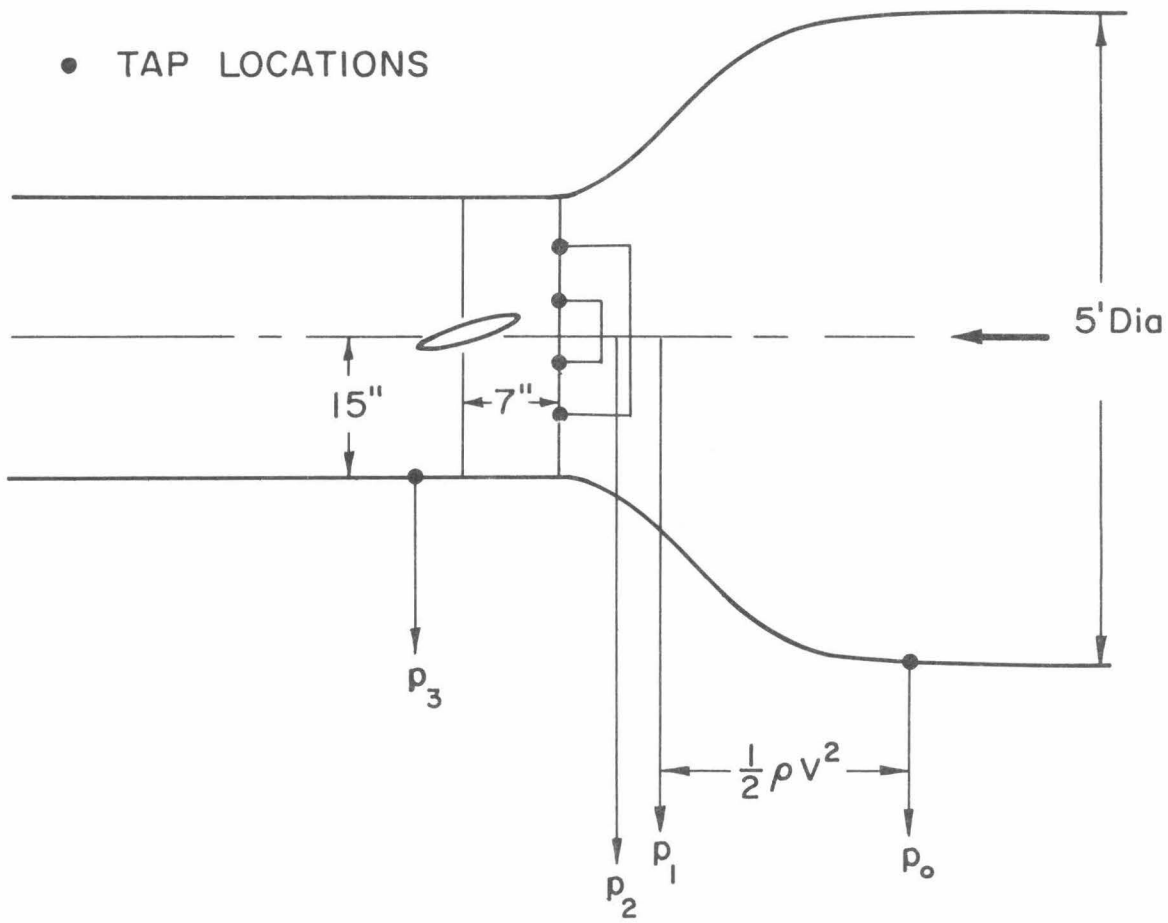

Figure 2 Location of pressure taps for the measurement of dynamic head and tunnel static pressures.

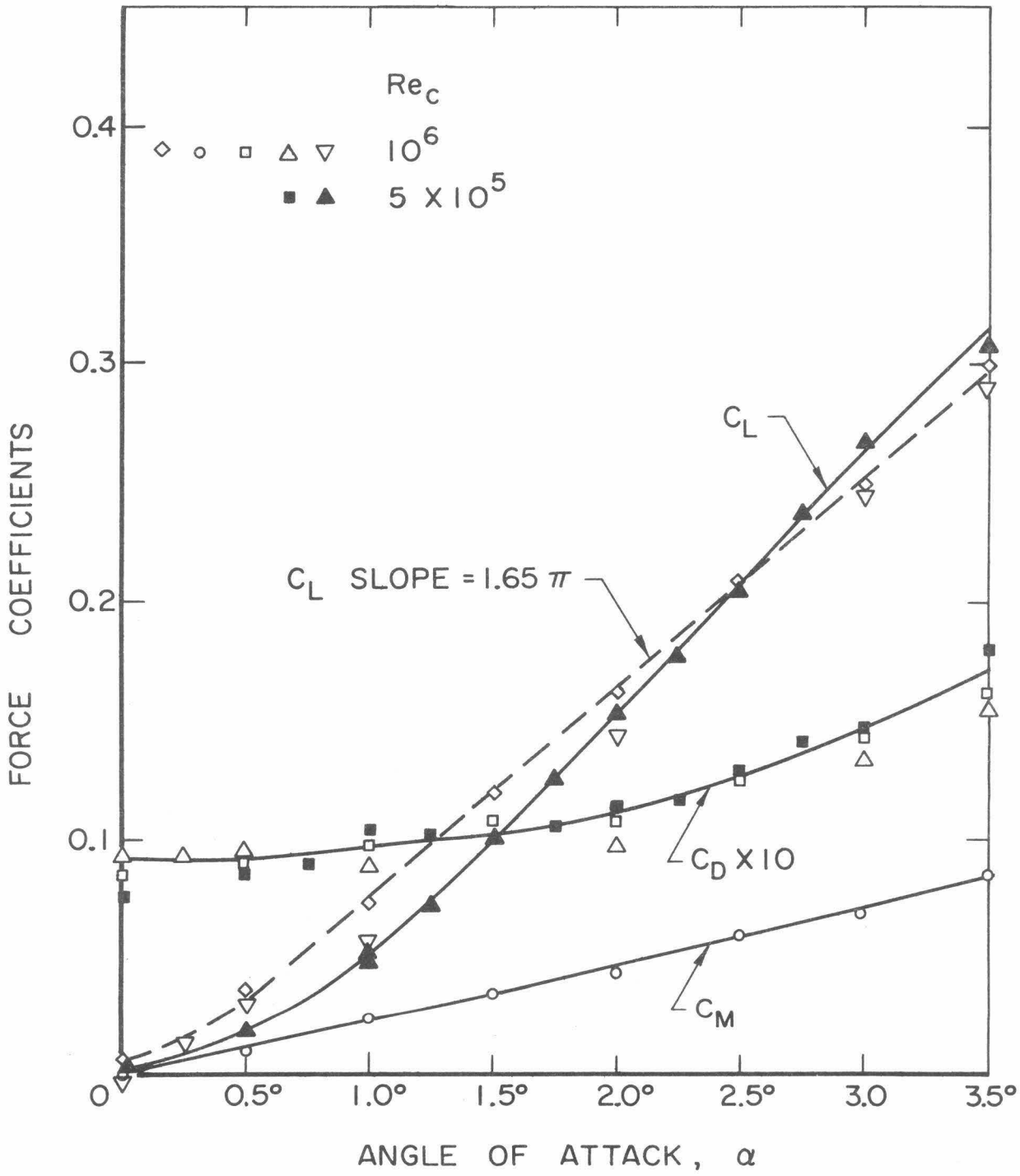

Figure 3 Force coefficients for the 3 inch model as a function of angle of attack with non-cavitating flow at two different Reynold's numbers.

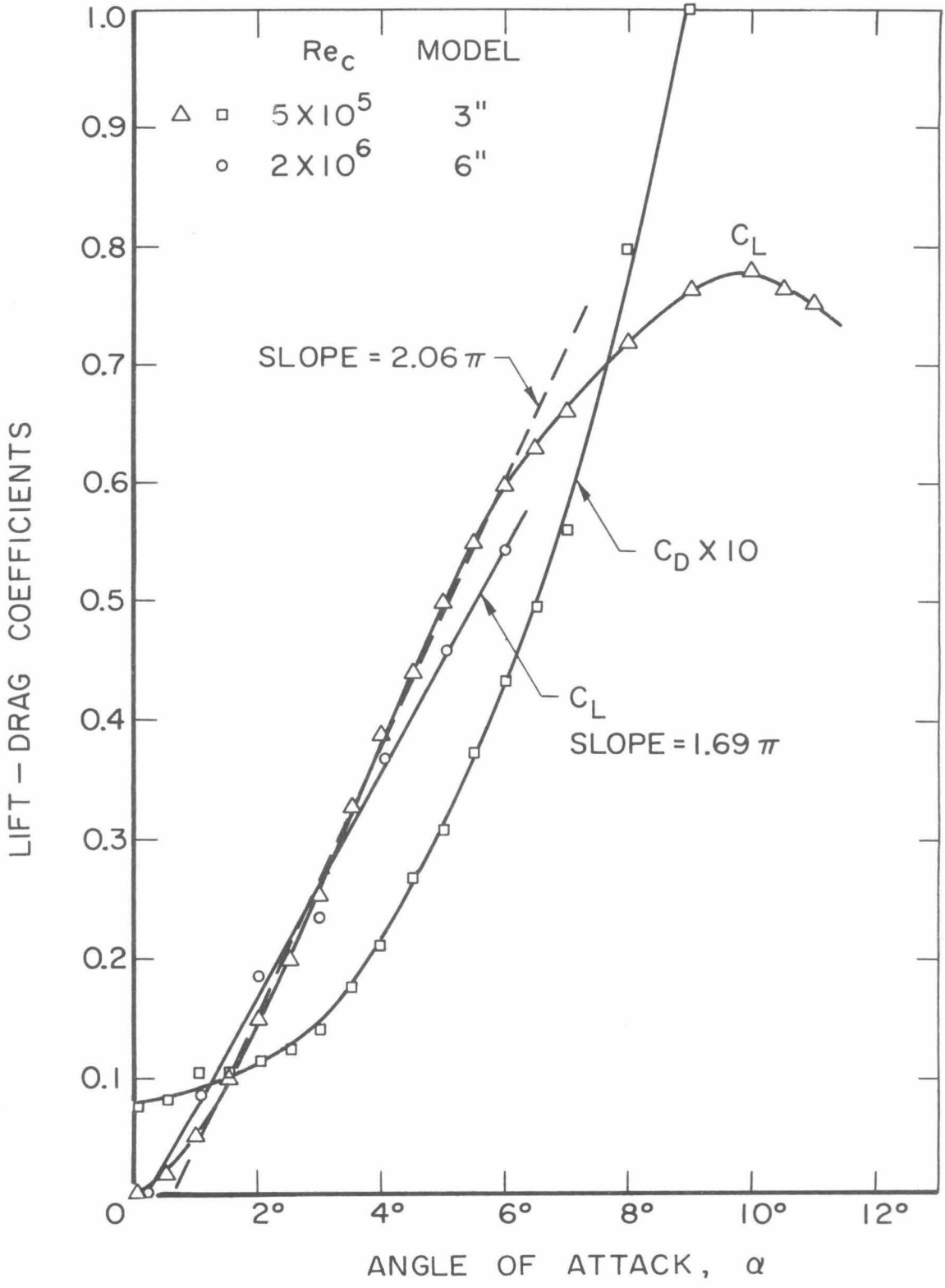

Figure 4 Variation of lift and drag coefficients with angle of attack for 3 inch model at Reynold's number of half million and variation of lift coefficient for 6 inch model with angle of attack under non-cavitating conditions.

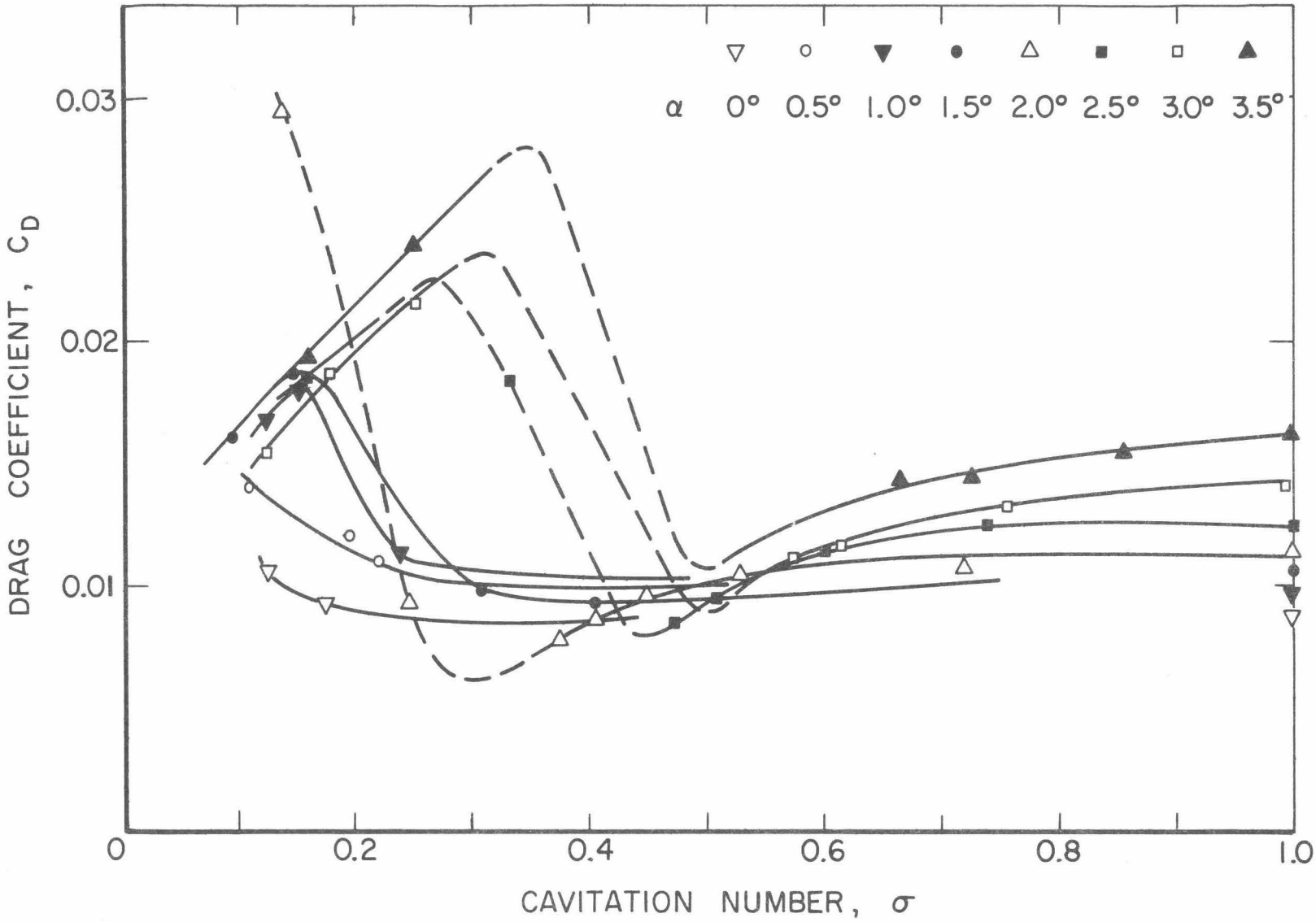

Figure 5 Variation of drag coefficient for 3 inch model with cavitation number and angle of attack.

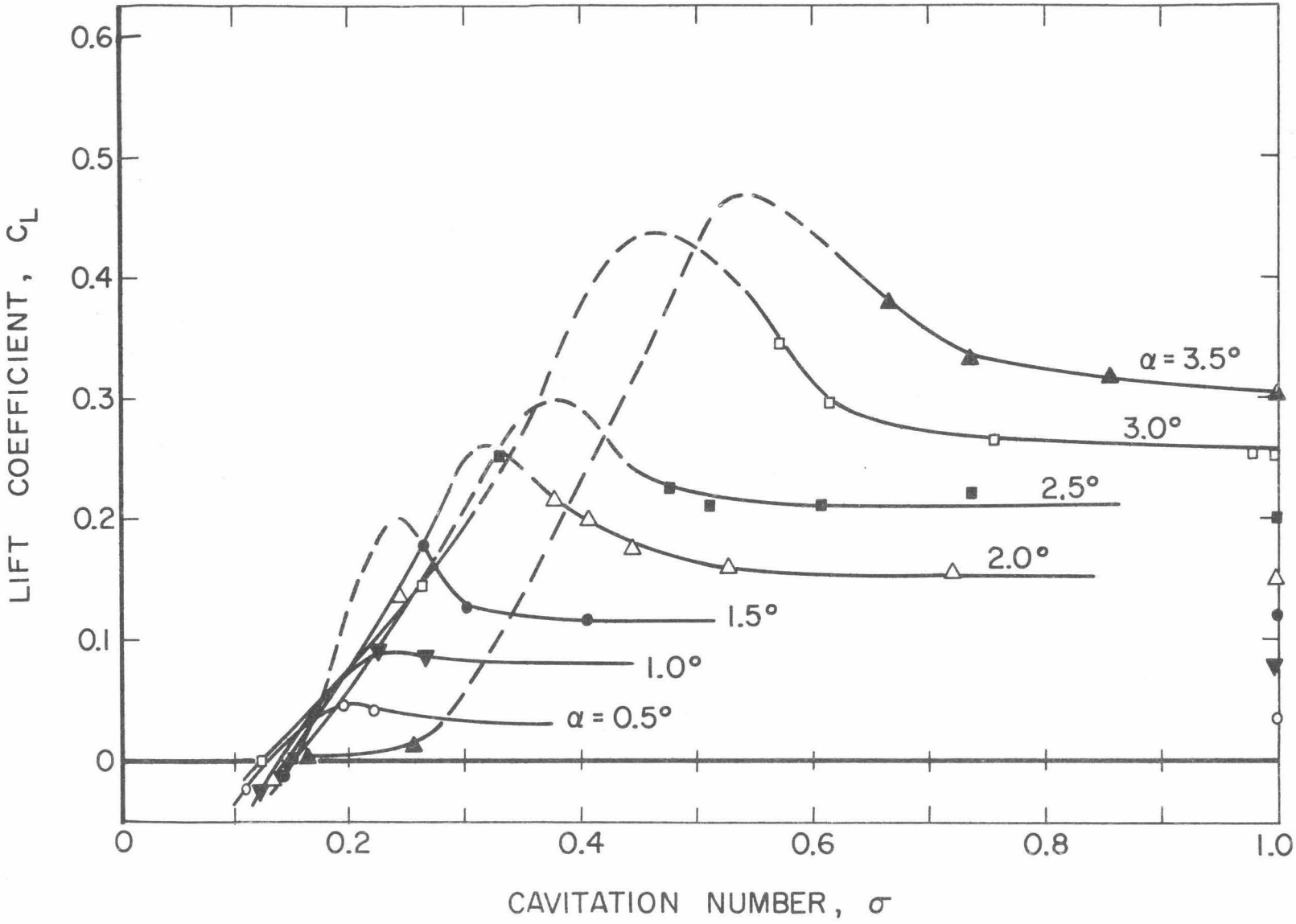

Figure 6 Variation of lift coefficient for 3 inch model with cavitation number and angle of attack.

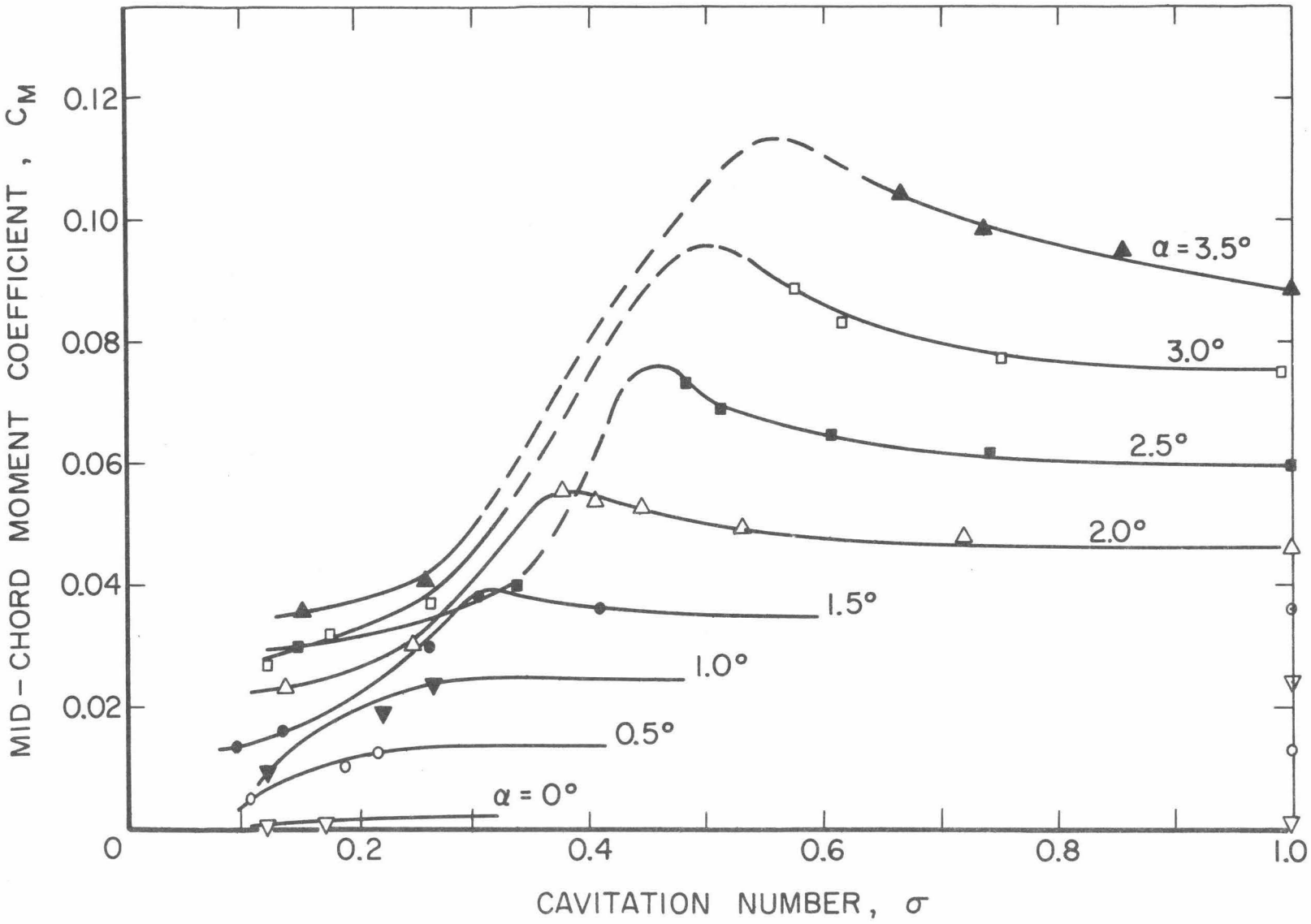

Figure 7 Variation of mid-chord moment coefficient with cavitation number and angle of attack.

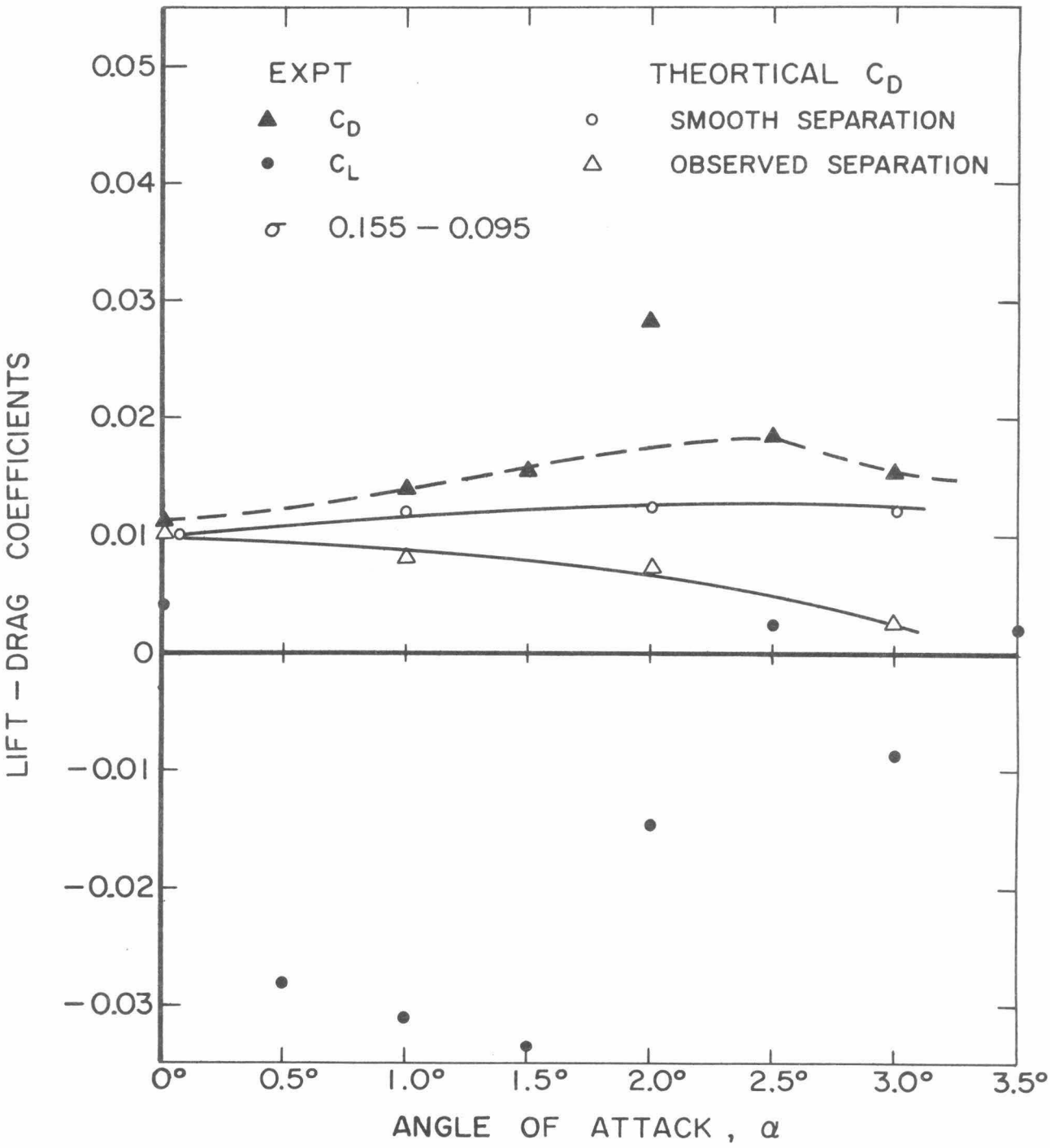

Figure 8 Comparison of experimental and theoretical drag coefficient and variation of experimental lift coefficient with angle of attack for low cavitation numbers.

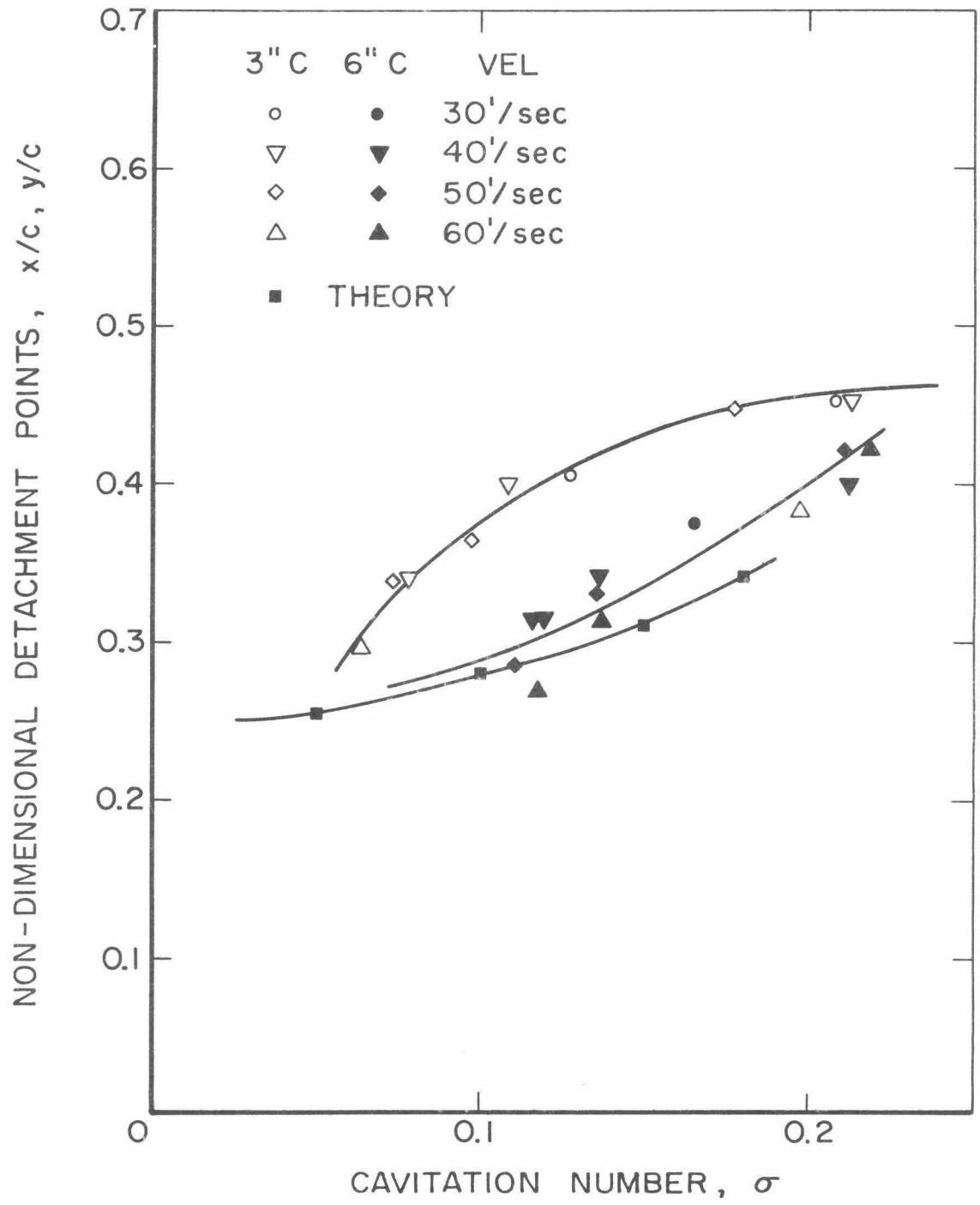

Figure 9 Variation of cavitation detachment point to chord ratio with model size, free stream velocity and cavitation number at zero degree angle of attack.

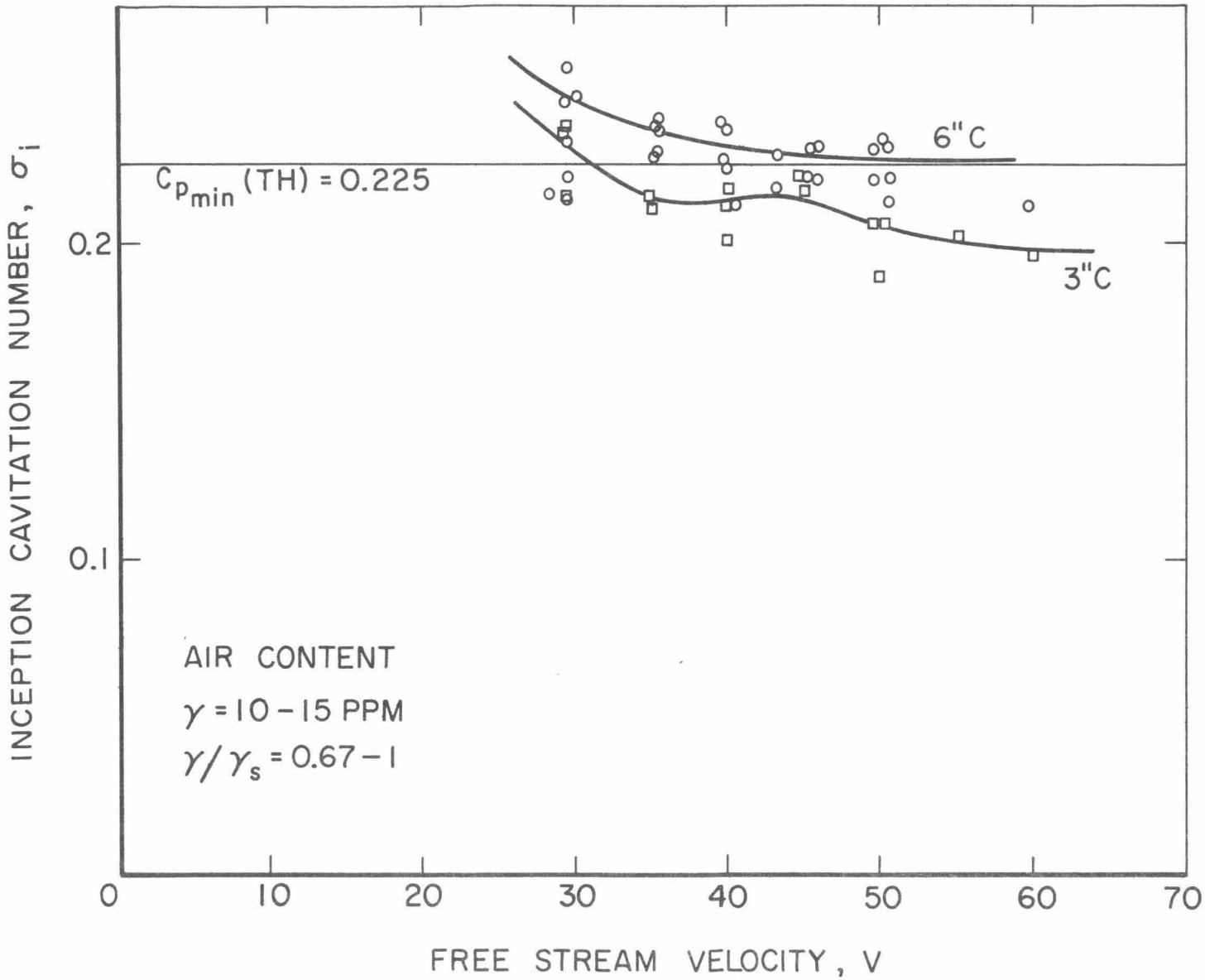

Figure 10 Variation of cavitation inception data with model size and free stream velocity at zero degree angle of attack.

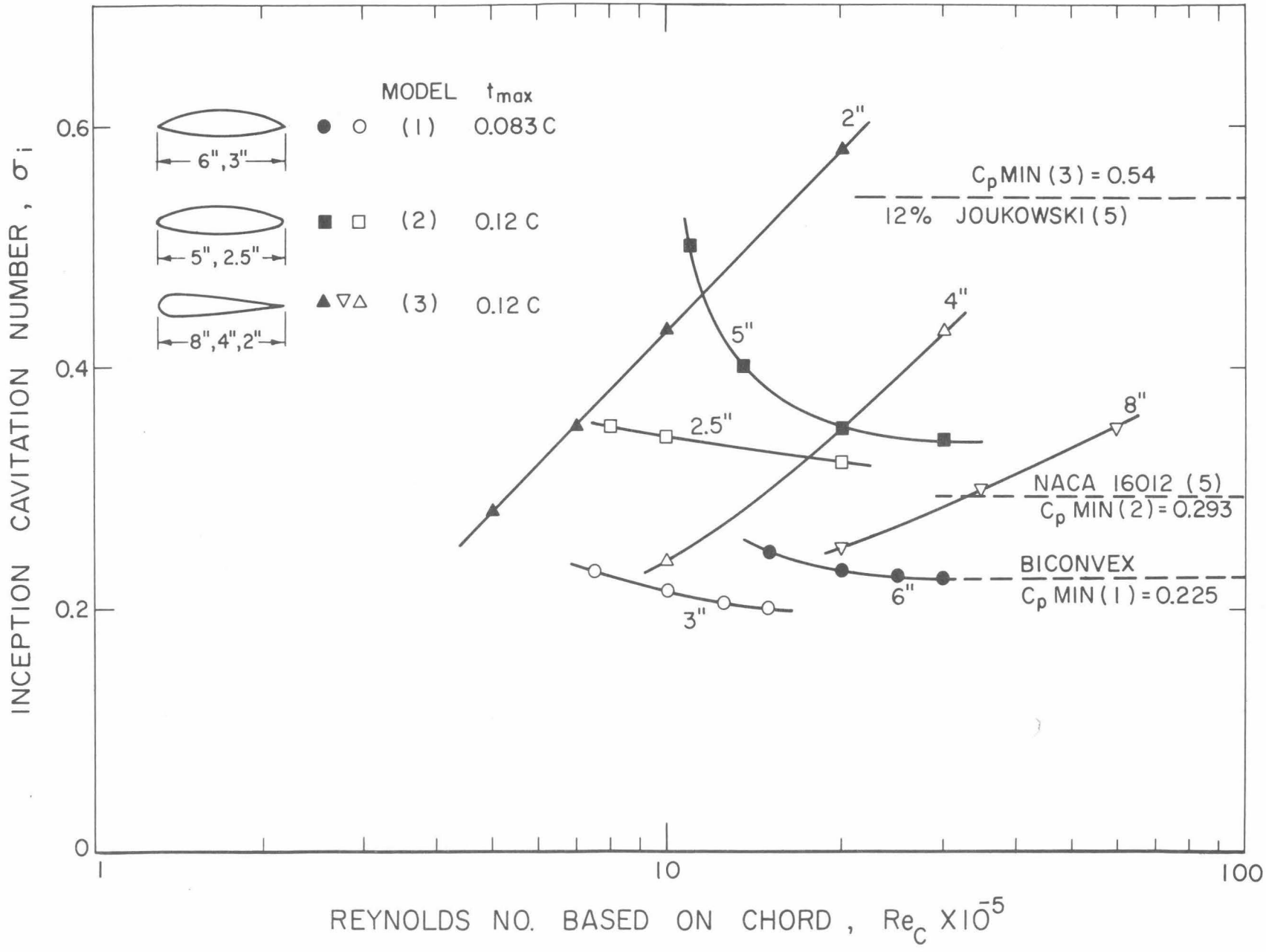

Figure 11 Comparison of cavitation inception data for different types of hydrofoils.

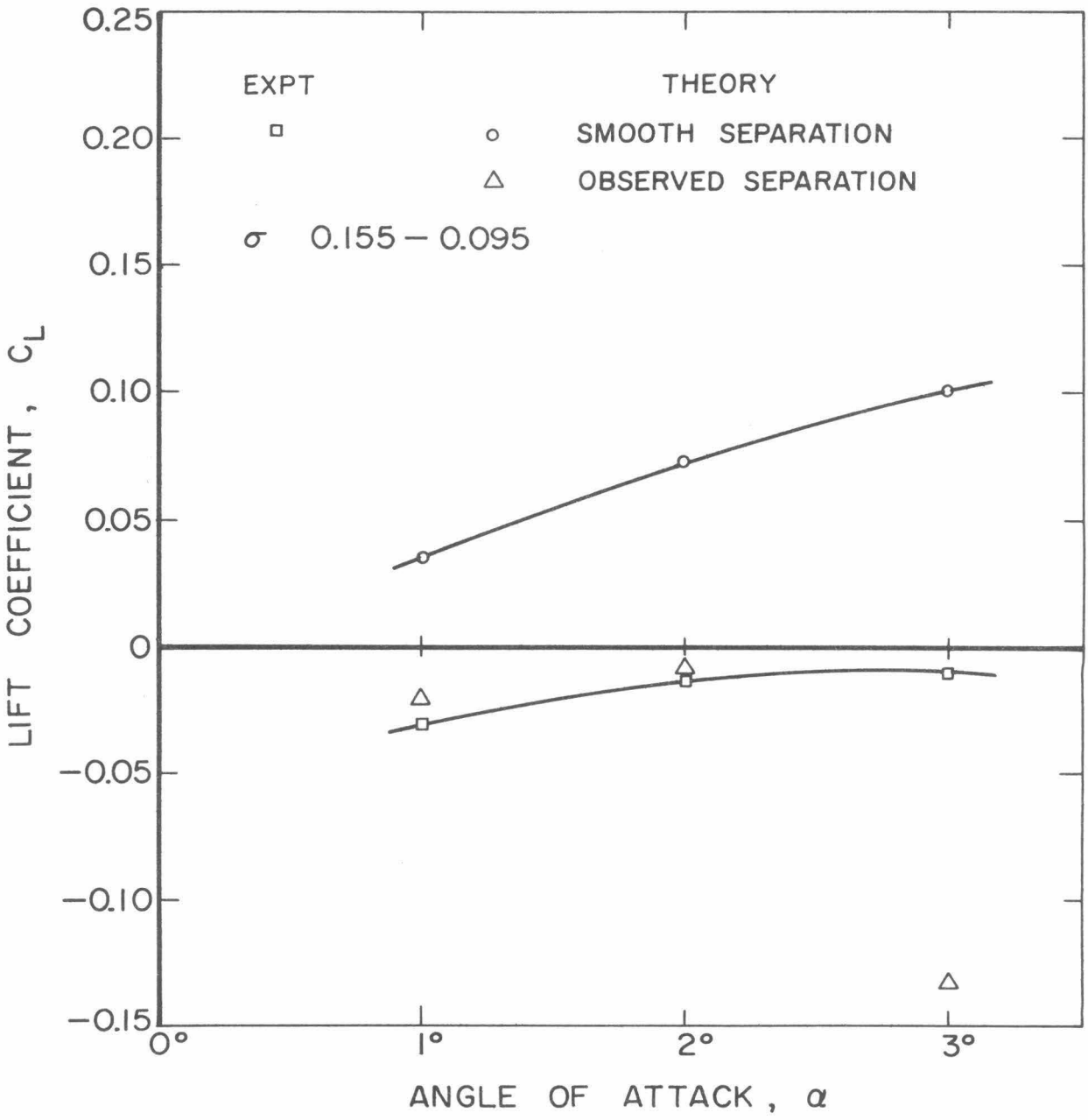

Figure 12 Comparison of experimental and theoretical lift coefficients for low cavitation numbers.

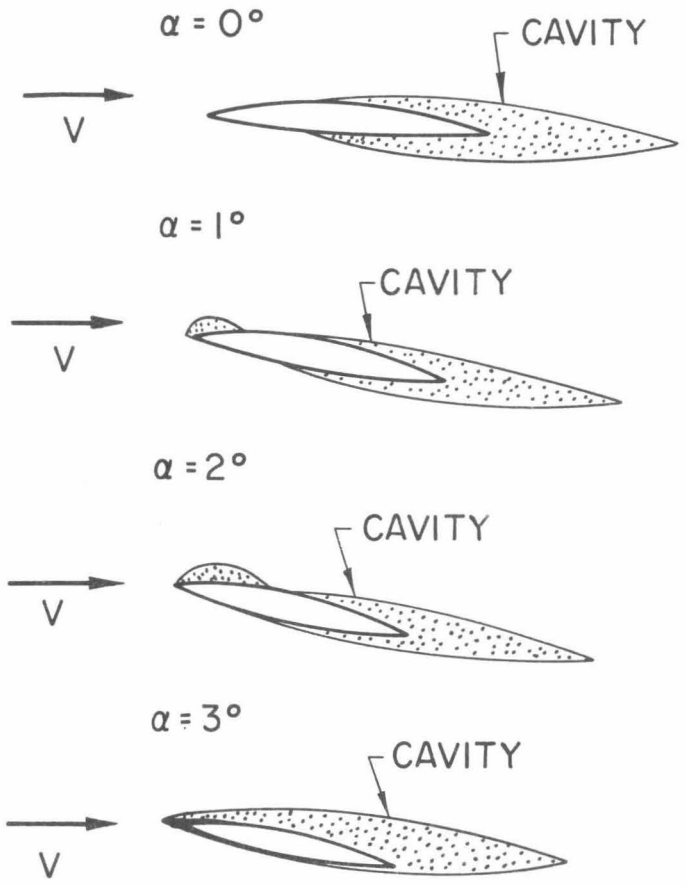

Figure 13 Sketch of the shift in cavitation detachment point on suction side of the foil with angle of attack.

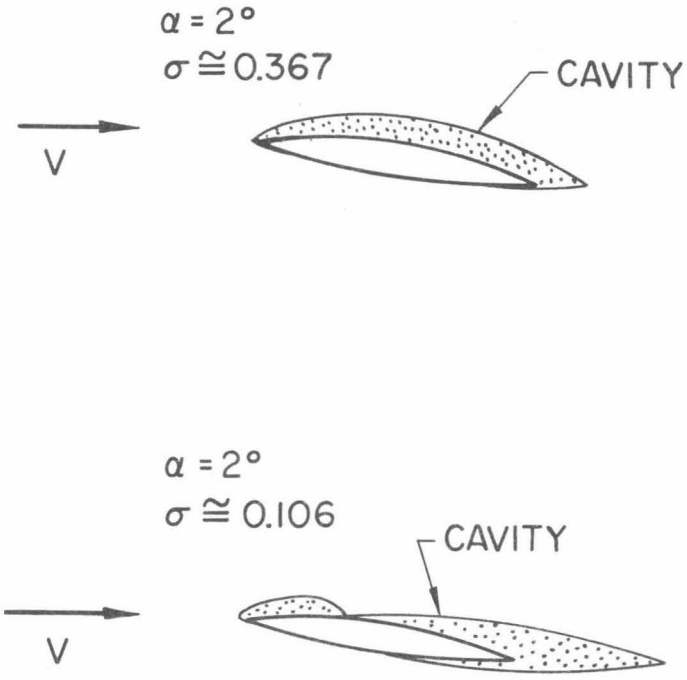

Figure 14 Sketch of the unique shift in cavitation detachment point on suction side of the foil with cavitation number at 2° angle of attack.

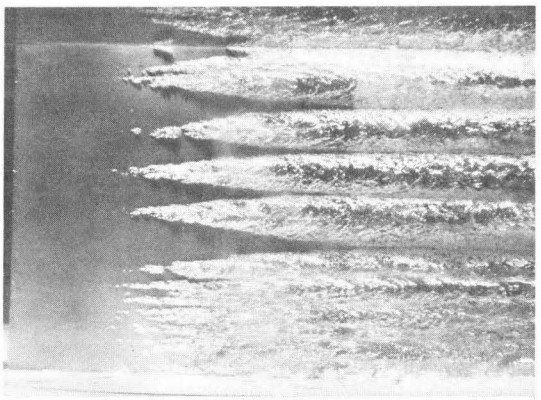

Figure 15 Illustration of a three dimensional pattern of nucleate streak cavitation detachment at zero angle of attack.

$V \doteq 51$ ft/sec, $\sigma \doteq .11$, $c = 6$ in.

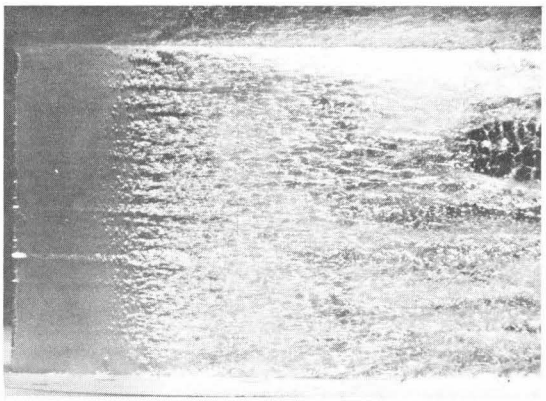

Figure 16 Illustration of nucleate bubble cavitation detachment on suction side at 1° angle of attack.

$V \doteq 40.4$ ft/sec, $\sigma \doteq .163$, $c = 6$ in.

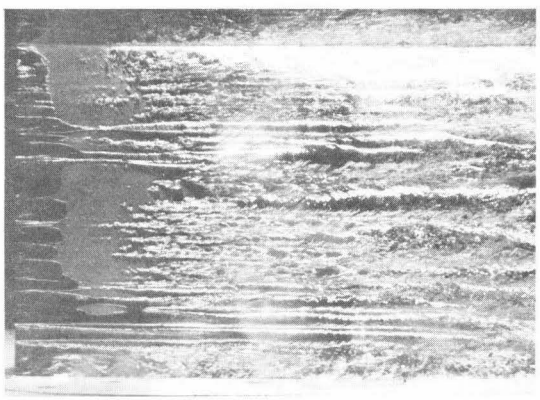

Figure 17 Cavitation pattern on suction side of the foil at 2° angle of attack with two cavities; one beginning from leading edge and another beginning from minimum pressure point.

$V \doteq 40.3$ ft/sec, $\sigma \doteq .106$, $c = 6$ in.

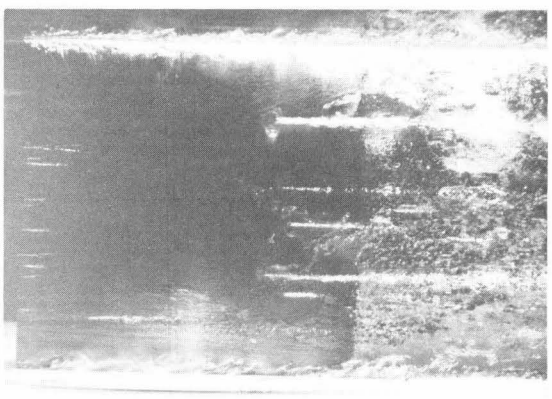

Figure 18 Cavitation pattern on suction side of the foil at 3° angle of attack with cavitation detachment from the leading edge.

$V \doteq 40.5$ ft/sec, $\sigma \doteq .114$, $c = 6$ in.

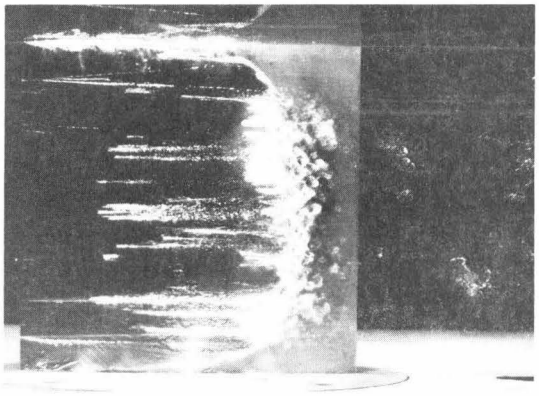

Figure 19 Illustration of partial cavity on suction side of the foil at 2° angle of attack with cavity beginning from leading edge.

$V \doteq 40$ ft/sec, $\sigma \doteq .367$, $c = 6$ in.

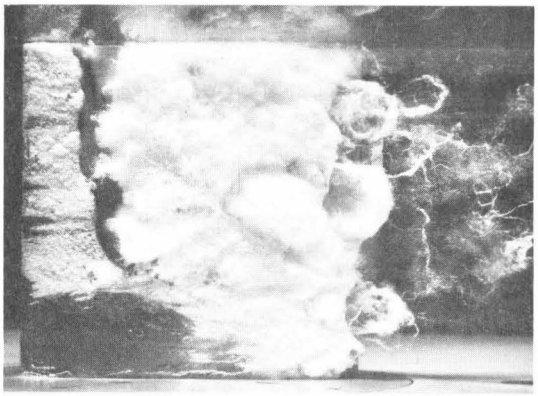

Figure 20 Cavitation pattern during the collapse cycle of an unsteady cavity on suction side of the foil at 5° angle of attack and with cavity length approximately equal to chord length.

$V \doteq 40.85$ ft/sec, $\sigma \doteq .634$, $c = 6$ in.

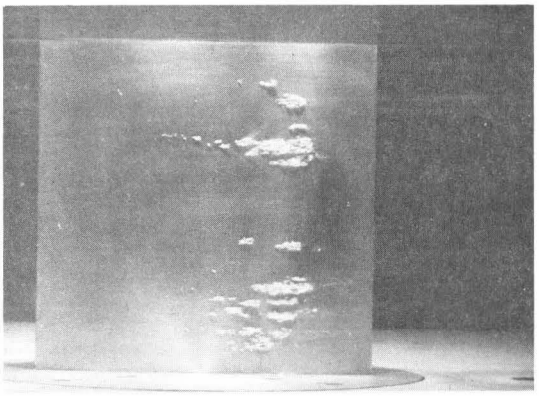

Figure 21 Illustration of cavitation pattern on 6 in. model at cavitation number slightly below the inception cavitation number.

$V \doteq 40.6$ ft/sec, $\alpha = 0°$, $\sigma \doteq .241$

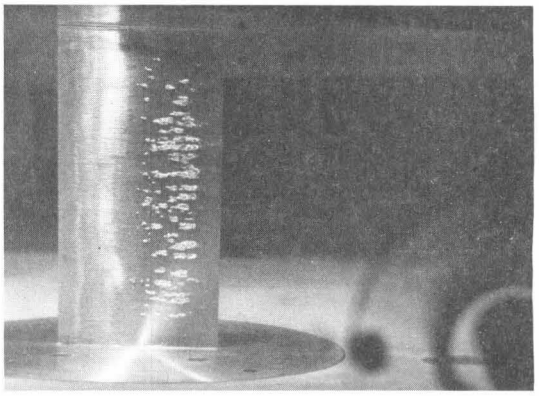

Figure 22 Illustration of cavitation pattern on 3 in. model at cavitation number slightly below the inception cavitation number.

$V \doteq 40$ ft/sec, $\alpha = 0°$, $\sigma \doteq .212$

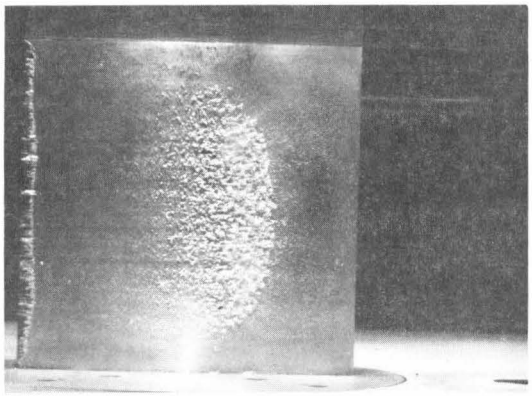

Figure 23 Illustration of cavitation inception on suction side of the foil at 1° angle of attack.

$V \doteq 40.4$ ft/sec, $\sigma \doteq .28$, $c = 6$ in.

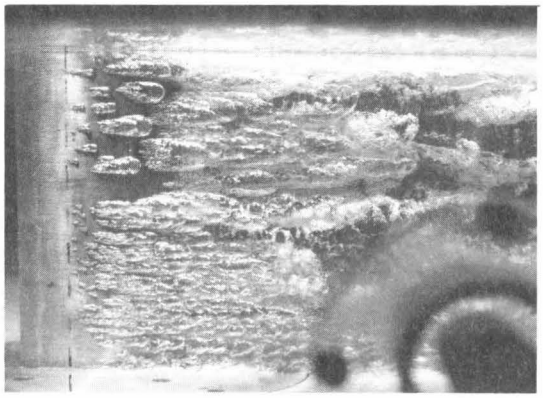

Figure 24 Illustration of nucleate bubble cavitation detachment on 3 in. foil at 50 ft/sec.

$V \doteq 50$ ft/sec, $\alpha = 0°$, $\sigma \doteq .077$

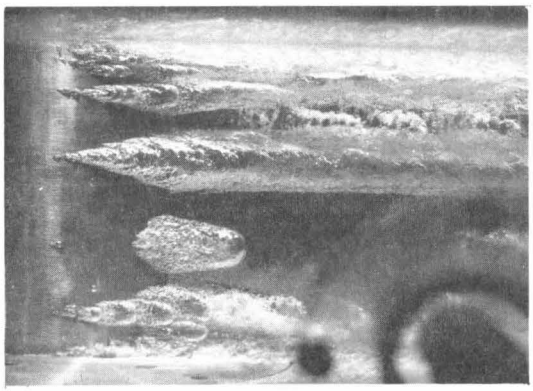

Figure 25 Illustration of shift in cavitation detachment type to nucleate streak as the velocity is increased to 60 ft/sec (compare Fig. 24).

$V \doteq 60$ ft/sec, $\alpha = 0°$

$\sigma \doteq .0631$, $c = 3$ in.

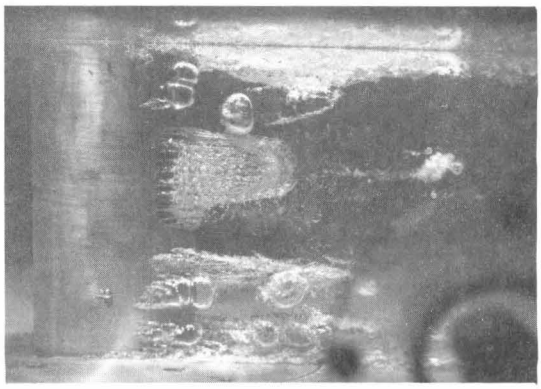

Figure 26 Illustration of mixed laminar and nucleate cavitation detachment on pressure side of the 3 in. foil at 1° angle of attack.

$V \doteq 40$ ft/sec, $\sigma \doteq .0814$, $c = 3$ in.

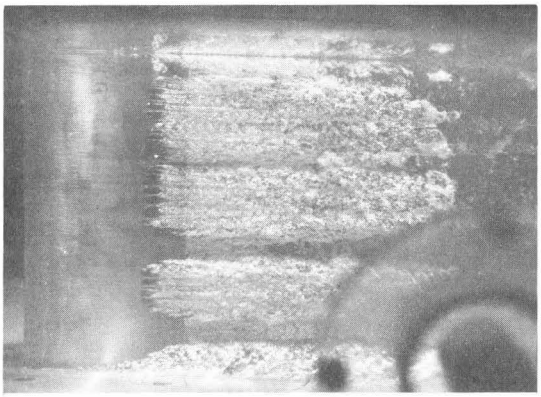

Figure 27 Illustration of laminar cavitation detachment on pressure side of the 3 in. foil at 2° angle of attack.

$V \doteq 40$ ft/sec, $\sigma \doteq .0955$, $c = 3$ in.

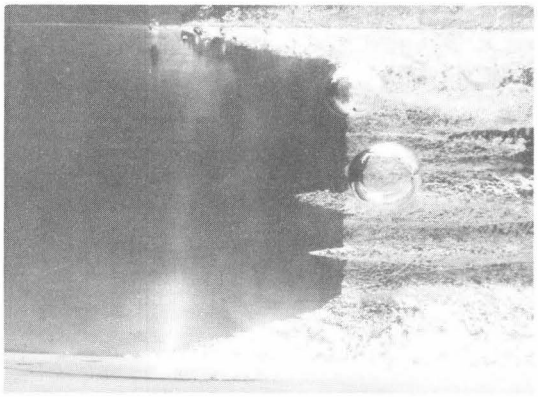

Figure 28 An example of non-uniform cavitation detachment on the pressure side of 6 in. foil at all angles of attack and high angles of attack for the 3 in. model.

$V \doteq 50$ ft/sec, $\alpha = +1°$,

$\sigma \doteq .0639$, $c = 6$ in.

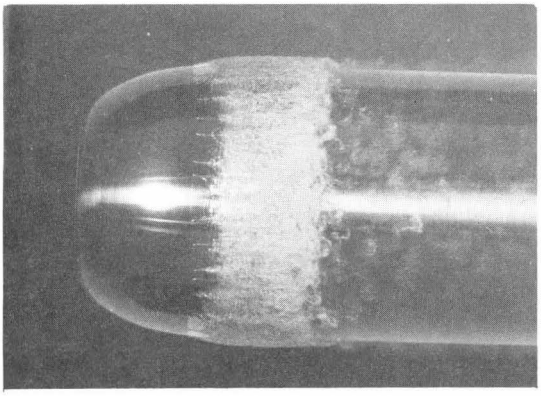

Figure 29 Illustration of laminar cavitation detachment on an axi-symmetric head taken from Ref. (12).

$V \doteq 60$ ft/sec, $\sigma \doteq .406$

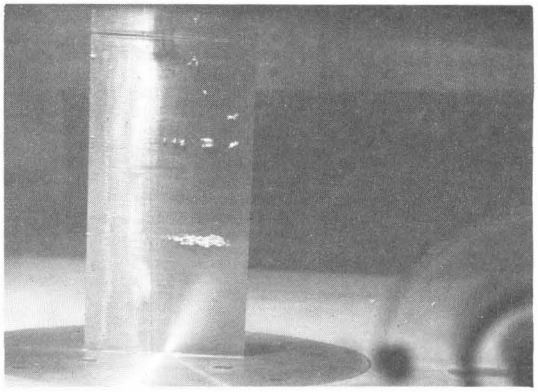

Figure 30 Illustration of leading edge disturbance influence on cavitation inception at low velocity for the 3 in. model.

$V \doteq 30$ ft/sec, $\alpha = 0°$, $\sigma \doteq .2075$

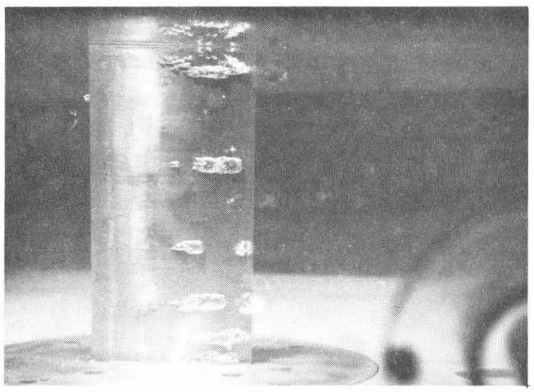

Figure 31 Cavitation pattern on the 3 in. foil at cavitation number slightly below the inception value at a velocity of 50 ft/sec.

$V \doteq 50$ ft/sec, $\alpha = 0°$, $\sigma \doteq .18$

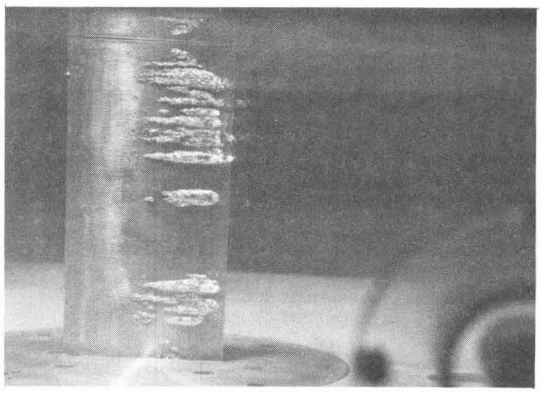

Figure 32 Streak type cavitation pattern on the 3 in. foil at cavitation number slightly below the inception value at a high velocity.

$V \doteq 60$ ft/sec, $\alpha = 0°$, $\sigma \doteq .2$

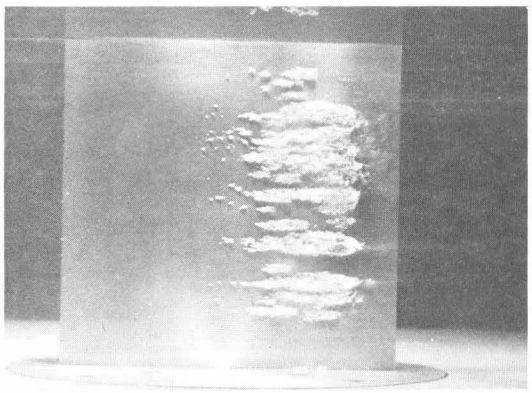

Figure 33 Streak type cavitation pattern on the 6 in. foil at cavitation number slightly below the inception value at a velocity of 50 ft/sec.

$V \doteq 50$ ft/sec, $\alpha = 0°$, $\sigma \doteq .212$

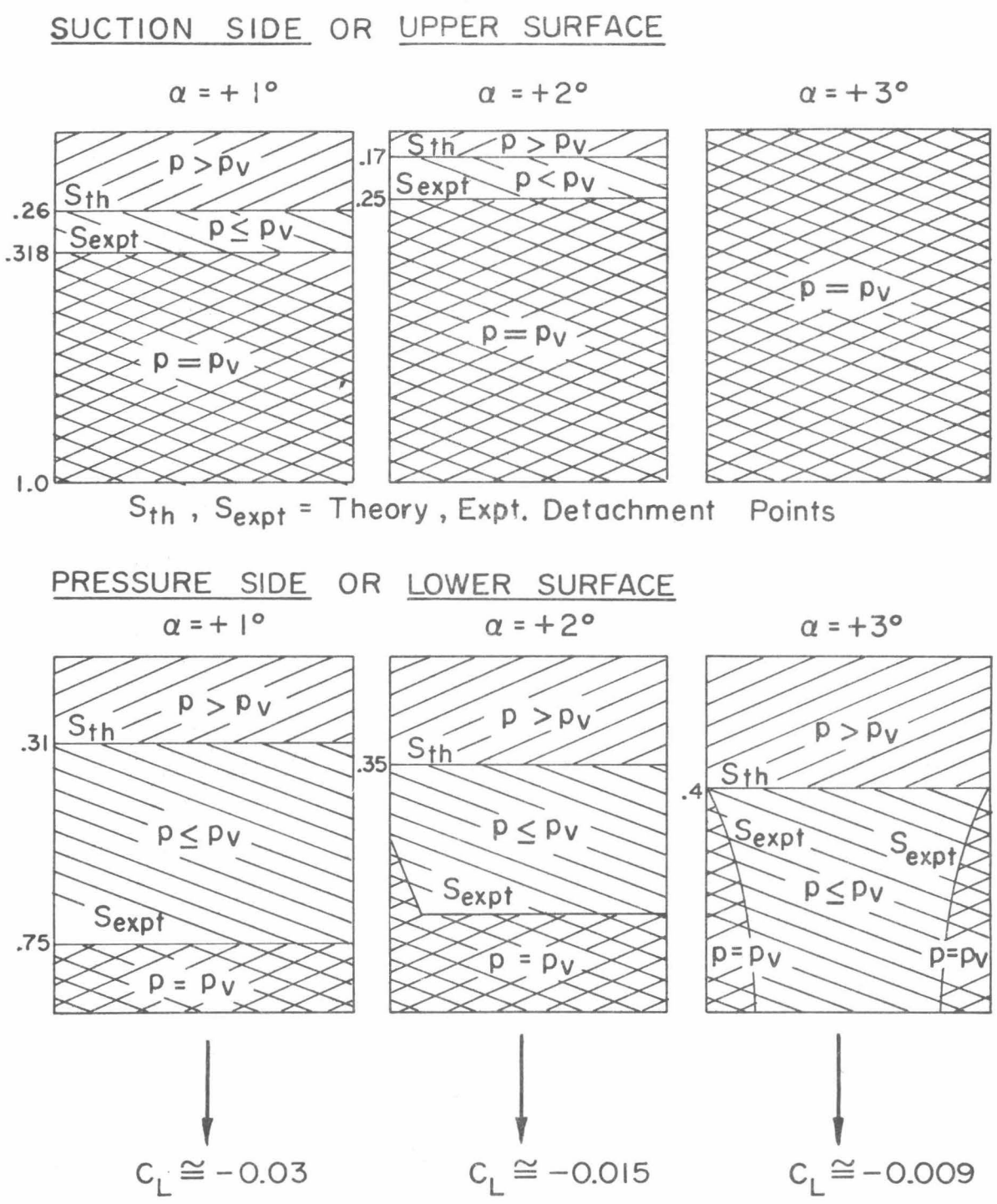

Figure 34 Illustration of pressure diagrams constructed with the use of photographs on suction and pressure sides of 3 inch model at angles of attack of 1°, 2° and 3° at low cavitation numbers. Cross hatched portions represent cavitating areas.

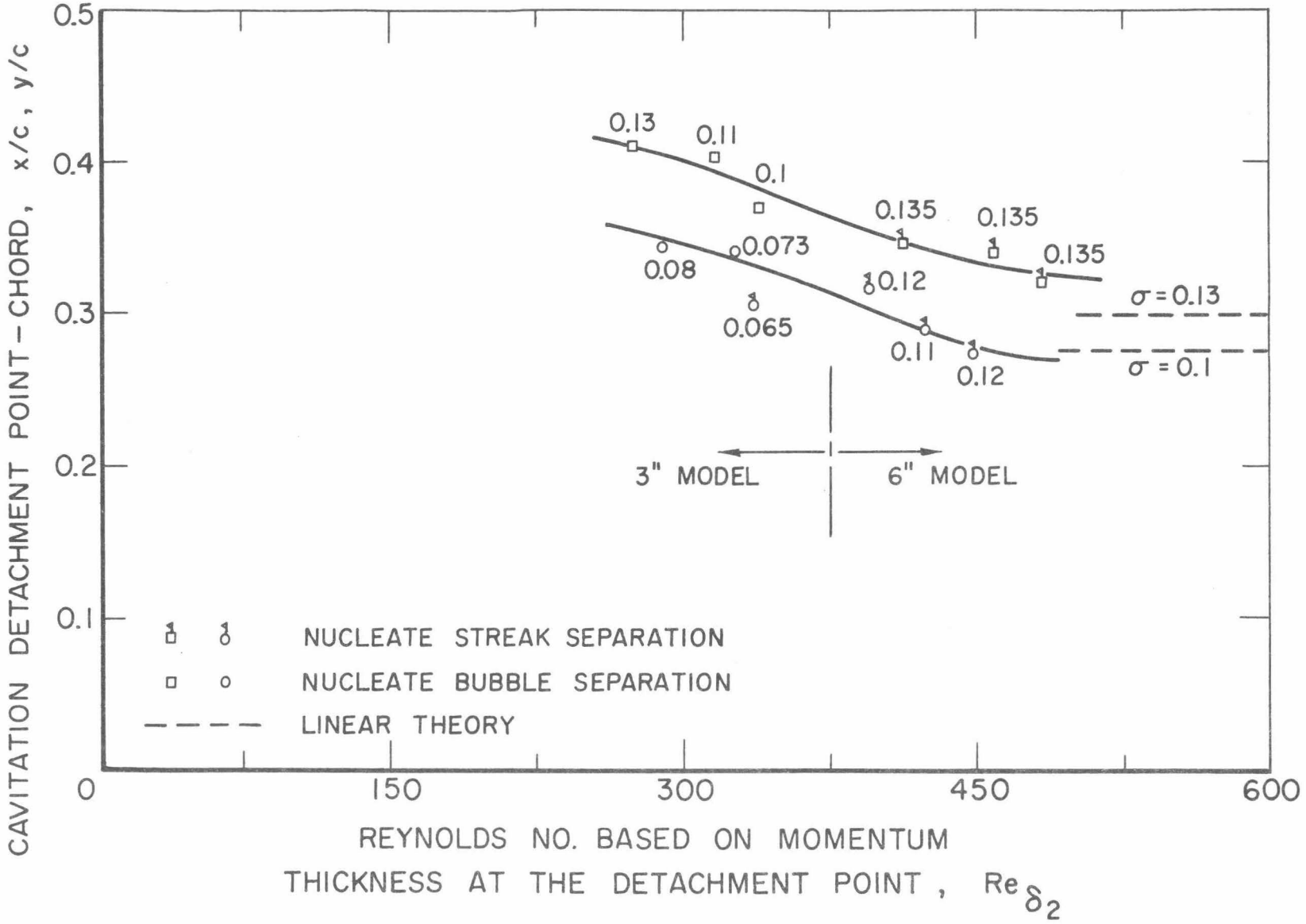

Figure 35 Variation of cavitation detachment point to chord ratio with Reynold's number based on momentum thickness at the detachment point and, cavitation number for the two models at 0° angle of attack.

TABLE 1

Comparison of theoretical and experimental separation data at various angles of attack.

		chord length	Theory		Experiment	
σ	α	c	x	y	x	y
.168	1^o	3"	.280		.364	
.14	1^o	3"	.260		.318	
.094	1^o	3"	.220		.318	
.083	2^o	3"	.17		.250	
.0746	1^o	3"	.220		.296	
.0814	1^o	3"		.31		.75
.0955	2^o	3"		.35		.727
.1635	1^o	6"	.280		.296	
.106	2^o	6"	.165		.227	

x - suction side detachment point
y - pressure side detachment point

APPENDICES

Appendix I

In this appendix we consider free streamline flow past a symmetrical lenticular strut with arbitrary separation points. The strut is described by an equation of the form $y = \eta(x)$ and fig. A1.1 describes the flow under consideration. The case of zero angle of attack was worked out by T. Y. Wu in unpublished work. In this case it was possible to work directly in the z-plane or the physical plane, but with the inclusion of angle of attack it is more convenient to work in a transformed plane.

FORMULATION OF THE PROBLEM

As in all cavity flows, we define cavitation number to be

$$\sigma = \frac{p_\infty - p_c}{\left(\frac{1}{2}\rho V^2\right)}$$

and this parameter characterizes the flow. Let q_c be the velocity on the cavity surface and this velocity will be chosen as the characteristic velocity for our purposes. Therefore the velocity vector may be written as

$$\overline{q} = \overline{q}_c(1 + u, v)$$

where u, v are the components of the dimensionless perturbation velocities in the x and y directions respectively. The linearization is done such that u^2, $v^2 << u$, v and the body-cavity system can be represented by a slit in the z-plane. Outside the body-cavity system the flow is assumed to be continuous, incompressable and irrotational.

Therefore it is sufficient to find the complex velocity $w(z)=u(z)-iv(z)$ which is analytic outside the body-cavity system which satisfies prescribed boundary conditions and singularities on the cavity-body system.

BOUNDARY CONDITIONS AND SINGULAR BEHAVIOR OF $w(z)$

(i) as $z \to \infty$. $\vec{q} = (V,O)$ hence using Bernoulli equation it can be shown that $w(z) = -\beta = -(1-(1+\sigma)^{-\frac{1}{2}})$ as $z \to \infty$.

(ii) Those portions of the slit which correspond to the wetted surface of the solid boundary must be streamlines

$$\therefore v^{+} = + \left(\frac{d\,\eta(x)}{dx}\right) - \alpha \text{ and } v^{-} = - \left(\frac{d\,\eta(x)}{dx}\right) - \alpha$$

α - angle of attack.

(iii) On the cavity surface $\bar{q} = q_c$ or $p = p_c$, using the linearized Bernoulli equation this corresponds to $u = O$ on cavity surface.

(iv) Body-cavity system must be equivalent to a single closed body, hence the closure condition requires that

$$\oint_{\Gamma} v(x, y)dx = 0 = \text{Im} \oint_{\Gamma} w(z)dz \ .$$

Γ is the circuit around the body-cavity system.

(v) The cavity pressure p_c is the minimum pressure in the neighborhood of the cavity boundary.

(vi) In the neighborhood of unknown separation points $z = c', d'$, the complex velocity potential $w(z)$ should be continuous and $|dv(x,o)/dx| < \infty$, the above condition implies that the curvature of the streamline, in linearized form, must be finite at the detachment (separation) points. For further discussion on this point see (7)*. These conditions are the linearized version of Brillion detachment conditions of nonlinearized

* Numbers in parenthesis refer to references at the end of the text.

free streamline theory. It should be realized that the actual flow in the neighborhood of separation points will be quite different due to real fluid effects as discussed earlier in the report and ref. (2).

(vii) and (viii) $w(z) \to \ln z$ as $z \to 0$ due to the included wedge angle of the leading edge and $w(z) \to \frac{A'}{\sqrt{z}}$ as $z \to 0$ due to angle of attack $A' =$ constant.

It should be mentioned that this condition gives rise to a singular pressure on suction side which would normally require a 2nd cavity. This cavity was in some cases observed. (See eg. fig. 17 of text.) This would greatly burden the analysis and it is felt that present lift and drag results would not be affected too much. In this respect problem formulation is not wholly consistent with free streamline theory. An example of a cavity flow past a body with two cavities is given by Cox and Clayden JFM (1958). Incidentally it is this feature that probably causes the slow convergence of the separation points in the calculations indicated later. At higher angles of attack the upper cavity springs from the leading edge and the problem disappears.

(ix) $w(z) \to N/\sqrt{z-\ell}$ as $z \to \ell$ $N =$ constant

The problem in the z-plane with the boundary conditions on the slit is shown in fig. A1.2.

It is conveniant to define a transformation $\zeta = a e^{i\pi} \sqrt{\frac{z}{\ell - z}}$ (1)

$$a = \sqrt{\ell - 1}$$

The transformation pulls the point $z = \ell$ to infinity and maps the entire flow field in to the lower half plane in the ζ plane. It should be

noticed that $z = \infty$ is mapped in to $\zeta = -ia$. The boundary value problem in the transformed plane is shown in fig. A1.3. This problem can now be formulated as Hilbert-problem by continuing $w(z(\zeta)) = W(\zeta)$ analytically to the upper half by the relationship

$$W(\bar{\zeta}) = -\overline{W(\zeta)}$$

in consequence we get

$$u(\xi, -\eta) = -u(\xi, \eta), \quad v(\xi, -\eta) = v(\xi, \eta)$$

or introducing the notation

$$W\pm(\xi) = W(\xi \pm io) = u(\xi, \pm o) - iv(\xi, \pm o) = u\pm(\xi) - iv\pm(\xi)$$

we have

$$W^+ + W^- = u^+ - iv^+ + u^- - iv^- = -2iv^-, \quad W^+ - W^- = u^+ - iv^+ - u^- + iv^- = 2u^+$$

using the above relationships the B.V.P. becomes

$$W^+ - W^- = 0 \text{ for } -\infty < \zeta < -c$$

$$W^+ + W^- = -2i(\eta'(\xi) - \alpha) \text{ for } -c < \zeta < 0$$

$$W^+ + W^- = -2i(\eta'(\xi) - \alpha) \text{ for } 0 < \zeta < d$$

$$W^+ - W^- = 0 \text{ for } d < \zeta < +\infty$$

The corresponding homogeneous problem is

$$H^+ - H^- = 0 \qquad \text{for } -\infty < \zeta < -c$$

$$H^+ + H^- = 0 \qquad \text{for } -c < \zeta < 0$$

$$H^+ + H^- = 0 \qquad \text{for } 0 < \zeta < d$$

$$H^+ - H^- = 0 \qquad \text{for } d < \zeta < +\infty$$

It can be easily verified that one solution for the above homogeneous problem is

$$H(\zeta) = \sqrt{(\zeta + c)(\zeta - d)}$$

to make $H(\zeta)$ single valued one can introduce a branch cut from $-c$ to d and the square root branch is chosen such that

$$H(\zeta) \to \zeta \text{ as } \zeta \to \infty$$

To find the particular solution define a function $G(\zeta)= \frac{W(\zeta)}{H(\zeta)}$, then one obtains a simpler problem for $G(\zeta)$ as follows.

$$G^+-G^- = \frac{W^+}{H^+} - \frac{W^-}{H^-} = \frac{W^+-W^-}{H^+} = 0 \qquad -\infty < \zeta < -c$$

$$G^+-G^- = \frac{W^+}{H^+} - \frac{W^-}{H^-} = \frac{W^++W^-}{H^+} = \frac{-2i(\eta'(\xi)-\alpha)}{H^+} \qquad -c < \zeta < 0$$

$$G^+-G^- = \frac{W^+}{H^+} - \frac{W^-}{H^-} = \frac{W^++W^-}{H^+} = \frac{-2i(\eta'(\xi)-\alpha)}{H^+} \qquad 0 < \zeta < d$$

$$G^+-G^- = \frac{W^+}{H^+} - \frac{W^-}{H^-} = \frac{W^+-W^-}{H^+} = 0 \qquad d < \zeta < +\infty$$

using Plemelj's formula (See eg. Muskhelishvili (8), p.42). One can write down the particular solution as

$$G(\zeta) = \frac{1}{2\pi i} \int_L \frac{G^+(\xi)-G^-(\xi)}{\xi-\zeta} d\xi$$

where L in this case is the real axis.

$$\therefore G(\zeta) = \frac{1}{\pi i} \int_0^d \frac{\eta'(\xi)+\alpha}{\sqrt{(\xi+c)(d-\xi)}} \frac{d\xi}{(\xi-\zeta)} + \frac{1}{\pi i} \int_{-c}^0 \frac{\alpha-\eta'(\xi)}{\sqrt{(\xi+c)(d-\xi)}} \frac{d\xi}{(\xi-\zeta)}$$

and $W_p(\zeta) = \sqrt{(\zeta+c)(\zeta-d)}\ G(\zeta)$

Complementary solution in general has the form of $W_c(\zeta)=H(\zeta)P(\zeta)$ where, $P(\zeta)=\sum_{n=-\infty}^{\infty} C_n \zeta^n$ with C_n being a complex constant.

To make the problem unique, $P(\zeta)$ should be chosen such that conditions (vii), (viii) and (ix) are satisfied, hence the form for $P(\zeta)$ has to be of the nature $P(\zeta) = \frac{(A+B\zeta)}{i\zeta}$ where A and B are real unknown constants. Therefore the complementary solution becomes

$$W_c(\zeta) = \left(\frac{A+B\zeta}{i\zeta}\right)\sqrt{(\zeta+c)(\zeta-d)}$$

and the complete solution $W(\zeta) = W_p(\zeta)+W_c(\zeta)$ becomes

$$W(\zeta)= \sqrt{(\zeta+c)(\zeta-d)}\left[\frac{1}{\pi i}\{I_1(\zeta)+I_2(\zeta)\}+\frac{A+B\zeta}{i\zeta}\right] \qquad (2)$$

where

$$I_1(\zeta)=\int_o^d \frac{\eta'(\xi)+\alpha}{\sqrt{(\xi+c)(d-\xi)}}\,\frac{d\xi}{(\xi-\zeta)}$$

and

$$I_2(\zeta)=\int_{-c}^{o} \frac{\alpha-\eta'(\xi)}{\sqrt{(\xi+c)(d-\xi)}}\,\frac{d\xi}{(\xi-\zeta)}$$

The condition (i) will determine the constants A and B, using this condition which states $W(\zeta) \to -\beta$ as $z \to \infty$, after some algebra one gets,

$$A=-a\left[\left(\frac{\beta}{D}\right)\sin\frac{(\psi-\varphi)}{2}+\frac{\mathrm{Im}\{I_1(-ia)+I_2(-ia)\}}{\pi}\right] \qquad (3)$$

$$B=\left(\frac{\beta}{D}\right)\cos\frac{(\psi-\varphi)}{2}-\frac{\mathrm{Re}[I_1(-ia)+I_2(-ia)]}{\pi} \qquad (4)$$

where

$$D=\left[(c^2+a^2)(d^2+a^2)\right]^{\frac{1}{4}}$$

$$\varphi=\tan^{-1}\left(\frac{a}{c}\right)$$

$$\psi=\tan^{-1}\left(\frac{a}{d}\right) \qquad (5)$$

and

$$\beta=\left[1-(1+\sigma)^{-\frac{1}{2}}\right]$$

Still ℓ, c, d are unknowns, but we have three conditions to determine them, namely closure and smooth separation at each of the detachment points.

For determination of ℓ consider the integral $I = \int_\Gamma w(z)dz$. Where Γ represents the circiut around body-cavity system. Since w(z) is analytic outside Γ excluding ∞, we can take any contour C_o which surrounds body-cavity system $\therefore I = \int_{C_o} w(z)dz$.

The contours Γ, C_o and corresponding contours L, L_o in ζ plane are shown in fig A1.4.

I can be rewritten as

$$I = \int_{-\infty-ib}^{\infty-ib} W(z(\zeta))\frac{dz}{d\zeta}d\zeta = \int_{-\infty-ib}^{\infty-ib} \frac{2\ell\zeta a^2}{(a^2+\zeta^2)^2} W(\zeta)d\zeta$$

or $$I = \int_{-\infty-ib}^{\infty-ib}(1+a^2)a^2 W(\zeta)\frac{d}{d\zeta}\left(-\frac{1}{a^2+\zeta^2}\right)$$

Integrating by parts we obtain

$$I = (1+a^2)a^2\left[\frac{-W(\zeta)}{a^2+\zeta^2}\right]_{-\infty-ib}^{\infty-ib} + a^2(1+a^2)\int_{-\infty-ib}^{\infty-ib}\frac{dW(\zeta)}{d\zeta}\frac{1}{a^2+\zeta^2}d\zeta$$

since $W(\zeta)\to\zeta$ as $\zeta\to\infty$, first term vanishes and thus

$$I = a^2(1+a^2)\int_{-\infty-ib}^{\infty-ib}\frac{dW(\zeta)}{d(\zeta)}\frac{1}{a^2+\zeta^2}d\zeta$$

since $\frac{dW(\zeta)}{d\zeta}\to 1$ as $\zeta\to\infty$ one can deform the contour to include the pt. $\zeta = -ia$ and the value of the integral is given by

$$I = a^2(1+a^2)\,[\text{Residue at } \zeta = -ia]$$

or $$I = \pi(a)(1+a^2)\left.\frac{dW(\zeta)}{d\zeta}\right|_{\zeta=-ia} \qquad (6)$$

Then the closure condition Im(I)=0 becomes

$$\mathrm{Im}\left(\frac{dW(\zeta)}{d\zeta} \mid \zeta = -ia\right) = 0 \tag{7}$$

Using the expression for $W(\zeta)$ and with some algebra one gets

$$\mathrm{Re}\left[\frac{dW}{d\zeta} \mid \zeta = -ia\right] = DI_5 \sin\frac{\psi-\varphi}{2} - D\cos\frac{\psi-\varphi}{2}\left(I_4 + \frac{A}{a^2}\right) + \frac{\beta}{2}\left(\frac{\cos\psi}{\sqrt{d^2+a^2}} - \frac{\cos\varphi}{\sqrt{c^2+a^2}}\right) \tag{8}$$

and

$$\mathrm{Im}\left[\frac{dW}{d\zeta} \mid \zeta = -ia\right] = -D\sin\frac{\psi-\varphi}{2}\left(I_4 + \frac{A}{a^2}\right)$$
$$-D\cos\frac{\psi-\varphi}{2} I_5 - \frac{\beta}{2}\left(\frac{\sin\psi}{\sqrt{d^2+a^2}} + \frac{\sin\varphi}{\sqrt{c^2+a^2}}\right)$$

where

$$I_4 = \mathrm{Re}\left[\frac{1}{\pi}\frac{d}{d\zeta}\{I_1(\zeta)+I_2(\zeta)\}\right]_{\zeta=-ia}$$

$$I_5 = \mathrm{Im}\left[\frac{1}{\pi}\frac{d}{d\zeta}\{I_1(\zeta)+I_2(\zeta)\}\right]_{\zeta=-ia}$$

and D, φ, ψ, are defined by (5). Using the expression for A from (3), closure condition becomes

$$\beta\left\{\frac{1}{2}\left[\frac{\sin\psi}{\sqrt{d^2+a^2}} + \frac{\sin\varphi}{\sqrt{c^2+a^2}}\right] - \frac{\sin^2\frac{\psi-\varphi}{2}}{a}\right\} =$$

$$-DI_5\cos\frac{\psi-\varphi}{2} - D\left(\sin\frac{\psi-\varphi}{2}\right)\left(I_4 - \frac{\mathrm{Im}[I_1(-ia)+I_2(-ia)]}{\pi a}\right) \tag{9}$$

Before proceeding to calculate c, d it is convenient to evaluate $I_1(\zeta)$, $I_2(\zeta)$, which can be evaluated in closed form. In present problem the term $\eta'(x)$ can be written as $\eta'(x)=a_o+bx$ or $\eta'(\xi)=a_o+\frac{b\ell\xi^2}{a^2+\xi^2}$.

Using the closed form expressions for $I_1(\zeta)$ and $I_2(\zeta)$ one can write $W(\zeta)$ as follows

$$W(\zeta) = \frac{\sqrt{(\zeta+c)(d-\zeta)}}{\pi}\left[\frac{ib\,\ell a}{2(\zeta+ia)}H(-ia) - \frac{ib\,\ell a}{2(\zeta-ia)}H(ia)\right.$$

$$\left.+\pi\left(\frac{A+B\zeta}{\zeta}\right)+\left(a_o+\frac{b\ell\zeta^2}{a^2+\zeta^2}\right)H(\zeta)\right]+\frac{\alpha}{\pi}\,\ell n(-1) \qquad (10)$$

where

$$H(\zeta) = \frac{2}{\sqrt{(\zeta+c)(d-\zeta)}}\,\ell n\,\frac{Z_1(\zeta)}{i\zeta(c+d)} \quad ,$$

$$Z_1(\zeta) = 2\sqrt{cd(\zeta+c)(d-\zeta)}+2cd+\zeta(d-c)$$

and $\ell n(-1) = -i\pi$.

It should be noted that superficially $W(\zeta)$ seems to be singular at $\zeta = \pm ia$ but using L'Hospital's rule it can be shown that $W(\zeta)$ is finite in the limit $\zeta \to \pm ia$ and so is $\frac{dW(\zeta)}{d\zeta}$ as $\zeta \to \pm ia$.

We now consider the determination of c, d, let us define

$$B'(\zeta) = \frac{1}{\pi}\left[\frac{ib\,\ell a}{2(\zeta+ia)}H(-ia) - \frac{ib\ell a}{2(\zeta-ia)}H(ia) + \pi\left(\frac{A+B\zeta}{\zeta}\right)\right]$$

and $$A'(\zeta) = a_o + \frac{b\ell\zeta^2}{(\zeta^2+a^2)}$$

Using above definitions we can write

$$\frac{dW(\zeta)}{d\zeta} = B'(\zeta)\left(\tfrac{1}{2}\right)\frac{(d-c-2\zeta)}{\sqrt{(\zeta+c)(d-\zeta)}} + \sqrt{(\zeta+c)(d-\zeta)}\,\frac{dB'(\zeta)}{d\zeta}$$

$$+\frac{2}{\pi}A'(\zeta)\left[\frac{dZ_1(\zeta)/d\zeta}{Z_1(\zeta)} - \frac{1}{\zeta}\right] + \frac{2}{\pi}\,\ell n\,\frac{Z_1}{i\zeta(c+d)}\cdot\frac{dA'(\zeta)}{d\zeta}$$

to find d we apply the condition (vi) at $d+0^+$, which states that $\left|\frac{dv(x, 0^+)}{dx}\right| < \infty$ in the neighborhood of d', but from the fact that $\frac{d\xi}{dx}$ is finite and $u^+ = 0$ for $\zeta > d+0^+$, the above condition is equivalent to $\left| \frac{dW(\zeta)}{d\zeta} \right|_{\zeta \to d} < \infty$ – (11), it is obvious that as $\zeta \to d$, $\frac{dB'}{d\zeta}$ and $\frac{dA'}{d\zeta}$ are finite but $\frac{dZ_1(\zeta)}{d\zeta}$ is singular like $\frac{1}{\sqrt{\zeta - d}}$.

Therefore in the limit as $\zeta \to d$ we can write

$$\frac{dW(\zeta)}{d\zeta}\Big|_{\zeta \to d} = \frac{1}{\sqrt{(\zeta + c)(d - \zeta)}} \left[\frac{B'(\zeta)(d-c-2\zeta)}{2} + \frac{2A'(\zeta)(d-c-2\zeta)}{Z_1(\zeta)} \right]_{\zeta \to d} + 0\left(\sqrt{d-\zeta}\right)$$

Hence for $\left|\frac{dW(\zeta)}{d\zeta}\Big|_{\zeta \to d}\right|$ to be finite we have to satisfy the following relationship which will be an equation for d.

$$\sqrt{d}\, B'(d)(c+d) + 4A'(d)\sqrt{c} = 0 \qquad (12)$$

similar argument for the separation point c leads to the equation

$$\sqrt{c}\, B'(-c)(c+d) + 4A'(-c)\sqrt{d} = 0 \qquad (13)$$

Now in principle one can determine the unknown quantities ℓ, c and d from equations (9), (12) and (13).

FORCE COEFFICIENTS: From linearized Bernoulli equations we have

$$C_p = \frac{p - p_c}{\frac{1}{2}\rho V^2} = -2(1+\sigma)u$$

now

$$C_L = \int_0^1 C_p\, dx = -2(1+\sigma) \int_0^1 u\, dx$$

or $$C_L = -2(1+\sigma)\,\mathrm{Re}\oint_\Gamma W(z)dz = -2(1+\sigma)\pi a\,(1+a^2)\,\mathrm{Re}\frac{dW(\zeta)}{d\zeta}\Big|_{\zeta=-ia} \qquad (14)$$

from the fact that u=0 on the cavity surface. Γ can be taken to be circuit around the body-cavity system. The quantity $\mathrm{Re}\,\frac{dW(\zeta)}{d\zeta}\Big|_{\zeta=-ia}$ is determined from equations (8) and (3).

It is well known [see for eg. (9)] that in linearized cavity flow analysis drag coefficient C_D is given by $C_D = 2\pi\,(1+\sigma)N^2$ (15) where N is the coefficient of the term $\frac{1}{\sqrt{z-\ell}}$ in the expansion of w(z) about $z = \ell$.

From the expression for $W(\zeta)$ (eqn. 10) and noting that behavior of $W(\zeta)$ as $\zeta \to \infty$ is equivalent to behavior of w(z) as $z \to \ell$ one obtains

$$\text{as } \begin{matrix}\zeta\to\infty \\ z\to\ell\end{matrix}\quad W(\zeta) \sim \frac{B\zeta}{i} \sim \frac{-Ba\sqrt{\ell}}{\sqrt{z-\ell}} \qquad \therefore N = -Ba\sqrt{\ell}$$

substituting this in equation (15) we have

$$C_D = 2\pi(1+\sigma)\,B^2a^2(1+a^2) \qquad (16)$$

RESULTS: Computations were done on the hydrofoil section described in the experimental part of this report. For this particular hydrofoil section $a_o = \left(\frac{19.2}{2}\right)\left(\frac{\pi}{180}\right)$, $b = -2a_o$. The procedure of computation was as follows, for given α, ℓ solve for c, d, β from equations (12), (13) and (9) by iteration, then obtain values for C_L and C_D from equations (14) and (16) respectively. The computations were carried up to angle of attack of 3^o and for various cavity length ℓ (or for various cavitation numbers σ). For angle of attack greater than 3^o, the numerical solution of equations (12) and (13) for c and d converged very slowly. At higher angles of attack ($\alpha > 3^o$) it would be preferable to fix value of c at the leading edge, then determine d from equation (12) and do the other calculations as before.

The results of computation are presented in figures A1.5, A1.6 and A1.7.

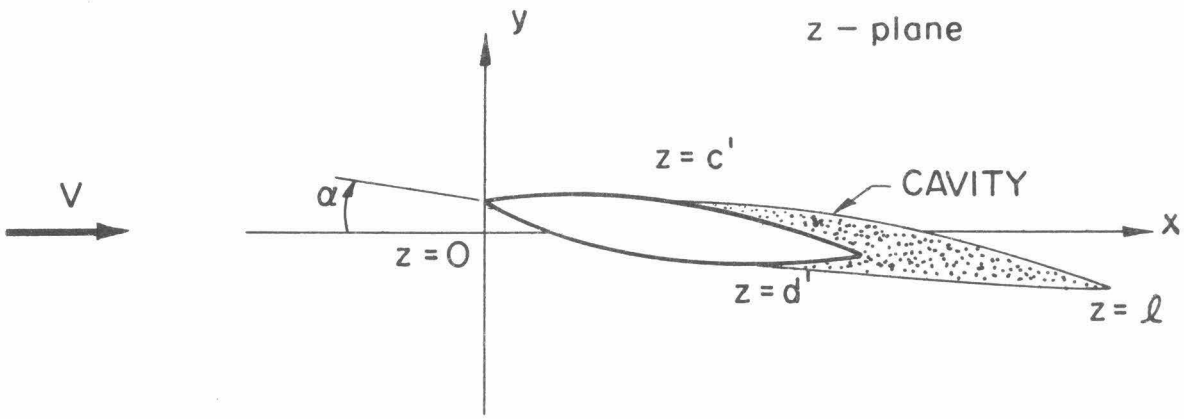

Figure A1.1 Flow configuration in the physical plane.

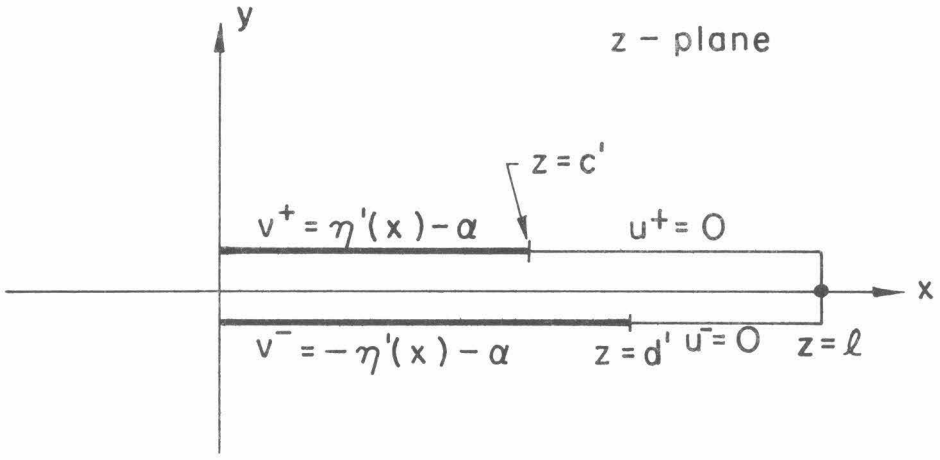

Figure A1.2 The Boundary Value Problem reduced to a slit in the z-plane.

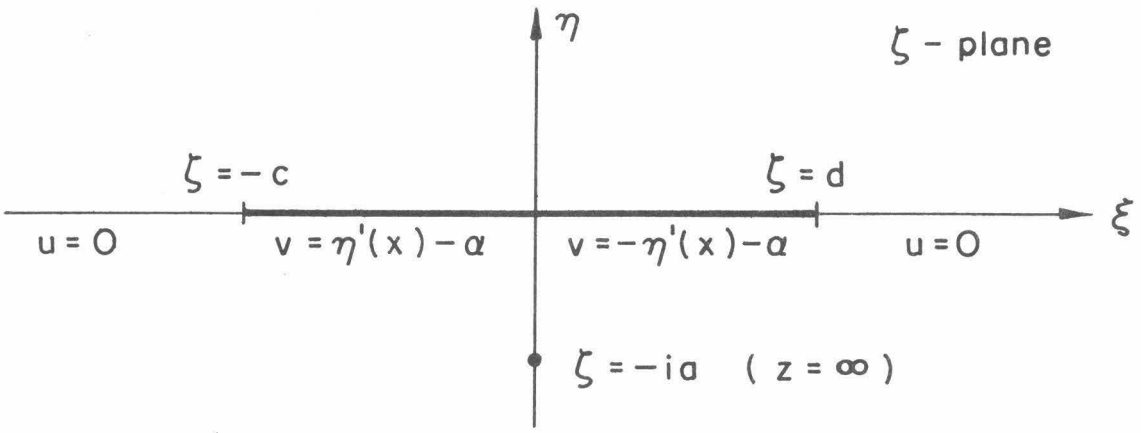

Figure A1.3 Transformed Boundary Value Problem in ζ-plane.

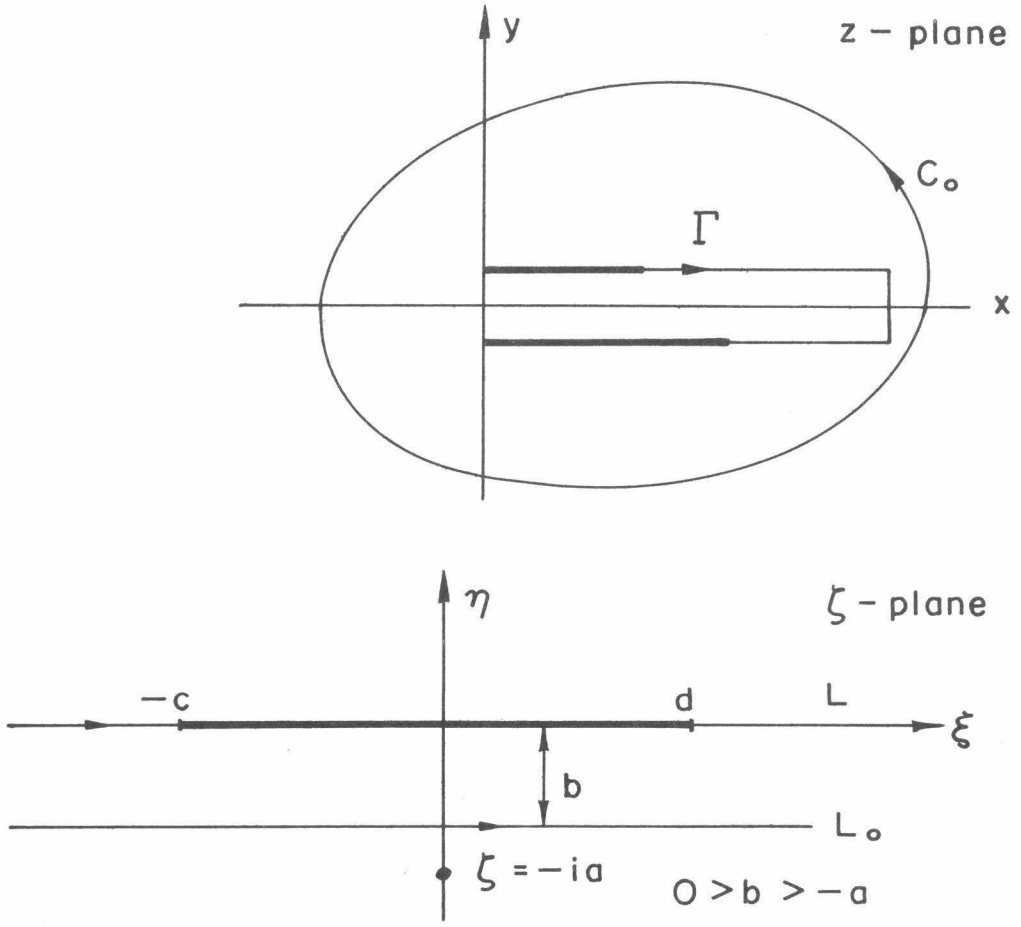

Figure A1.4 Transformation of contours Γ and C_o in z-plane to contours L and L_o in ζ-plane.

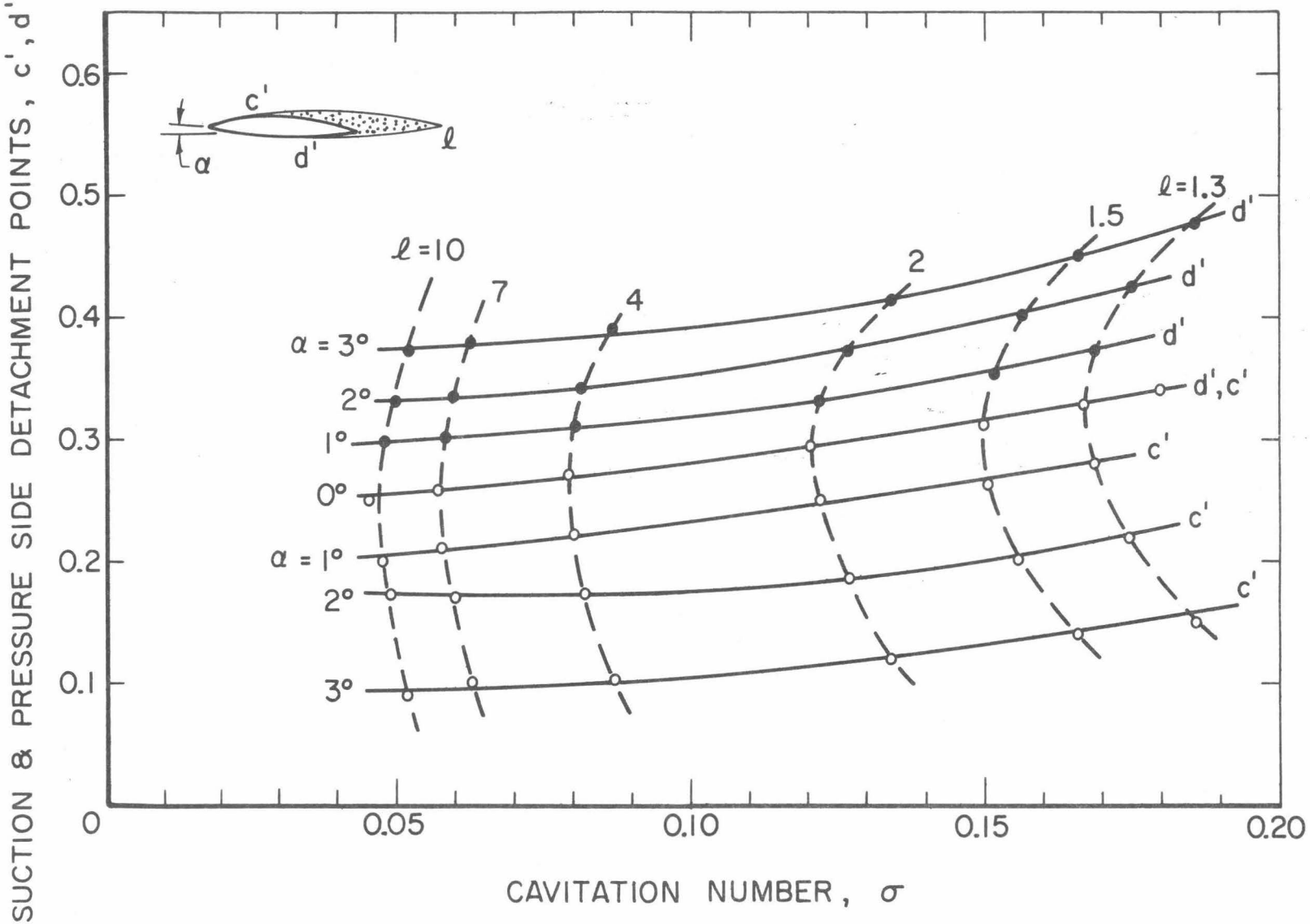

Figure A1.5 Variation of suction side detachment point c′ and pressure side detachment point d′ as function of angle of attack and cavitation number.

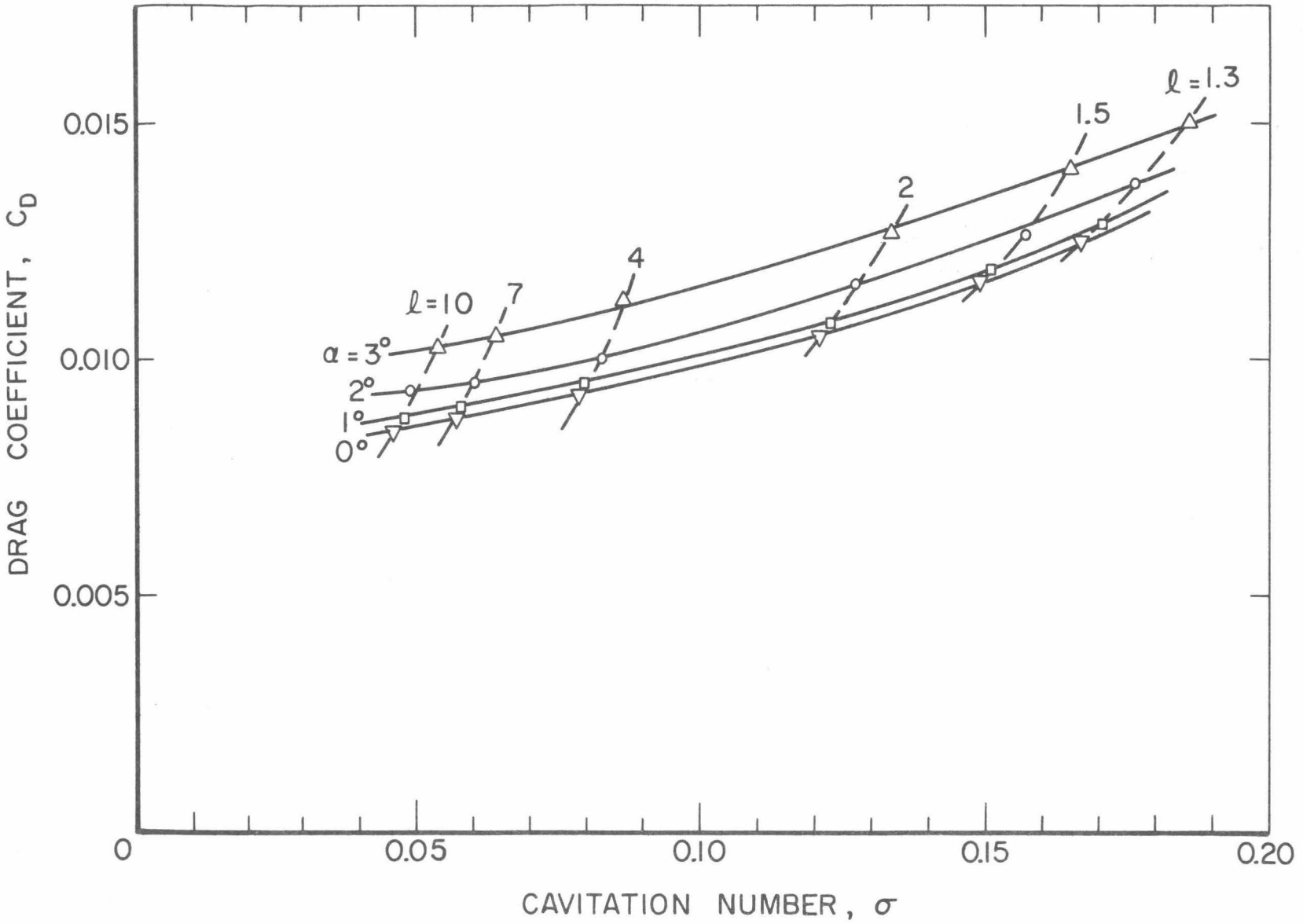

Figure A1.6 Variation of theoretical drag coefficient as function of angle of attack and cavitation number.

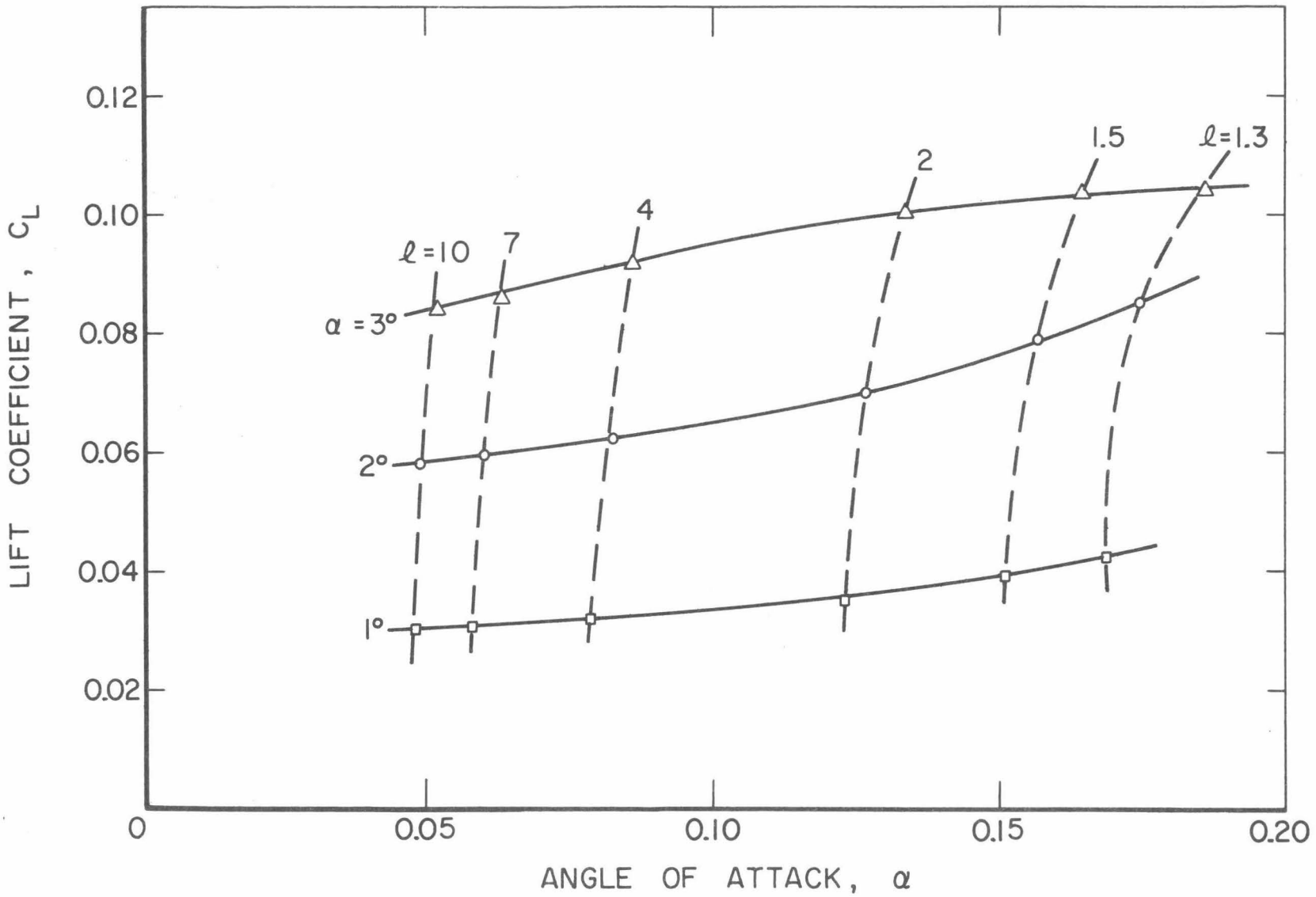

Figure A1.7 Variation of theoretical lift coefficient as function of angle of attack and cavitation number.

Appendix 2

In this section the method and results of the flow visualization technique using an oil film are discussed.

Procedure. After many trials, mixture of red lead oxide and oil with a ratio of 10:4 was chosen as the oil film medium. A thin coating of this mixture was applied on the model and the desired velocity of 20 ft/sec was obtained as rapidly as possible. The tunnel velocity was maintained at this value for about 20 minutes. During this period careful visual observation was done and four to five flash photographs of the oil film pattern were obtained. The procedure was repeated for various angles of attack. This procedure could not be used to visualize the flow at 40 ft/sec, since by the time this high velocity was reached most of the oil film coating was worn off.

Discussion of Results. The photographs taken during the test runs were in color, and black and white reproduction of the same did not show very much of the flow pattern. For this reason no photographs are included in the appendix but a description of each is given with diagrams constructed from the photographs for illustration purposes.

At zero angle of attack considerable amount of paint was left over at the downstream end of the hydrofoil, which is an indication of flow separation even though no trace of reverse flow in the separated zone was apparent. Some amount of paint was left over near the intersection of the hydrofoil and tunnel wall; apparently the effect of tunnel wall boundary layer is to induce local flow separation or thicken the local boundary layer on the hydrofoil adjacent to the wall. These localized effects due to wall boundary layer could influence the forces experience by the model. The

effect of Reynold's number on these localized effects was not investigated. An illustration of the above description is shown in Fig. A2.1. At .5° angle of attack on the pressure side some paint was left over near the leading edge of the hydrofoil due to the stagnation region of the flow. Some paint was left over at the trailing edge portion also; which is thought to be due to the presence of a thick boundary layer. The effect of tunnel walls was less pronounced than zero degree case. At 2.5° angle of attack on the pressure side the flow pattern left over was very similar to that at .5° angle of attack, except for lesser amount of paint being left over at the trailing edge portion of the foil and a more pronounced tunnel wall boundary layer effect. At .5° angle of attack on the suction side, paint was left over at the leading edge area due to the local laminar separation bubble. The effect of clearance between the model and tunnel wall was to wear off paint slower near the tip area than other areas of the foil. Similar effect was noticed due to the effect of tunnel wall boundary layer. At 2.5° angle of attack on the suction side, the flow pattern was very similar to .5° degree case. At 5° angle of attack on the suction side, clear indication of reverse flow in the locally separated laminar bubble near the leading edge was visible. The effect of tip clearance became much more pronounced leaving a three dimensional flow pattern on the foil surface. Figure A2.2 tries to illustrate this phenomena.

Figure A2.3 shows a sketch derived from visual observations and indicates the effect of leading edge disturbances on boundary layer characteristics downstream of these disturbances. The effect is to create patches of flow which are turbulent with laminar flow in between them. Depending on the size of the leading edge disturbance the turbulent patch would begin

either right from the disturbance or further downstream as indicated in the figure.

Conclusion. Due to experimental difficulties the effect of Reynold's number on the flow pattern past the hydrofoil could not be studied. Due to interaction of tunnel wall boundary layer with the boundary layer on the hydrofoil localized low pressure regions are created, this could have effects on the forces experienced by the model and cavitation pattern on the model. The presence of laminar separation bubble at the leading edge and subsequent reattachment of the flow on the suction side of the hydrofoil at a low angle of attack of $.5^{o}$ and higher angles was observed. The effect of leading edge disturbances was to create turbulent flow patches in otherwise laminar flow field. Separation of flow on pressure side at angles of attack of $.5^{o}$ and 2.5^{o} could not be ascertained.

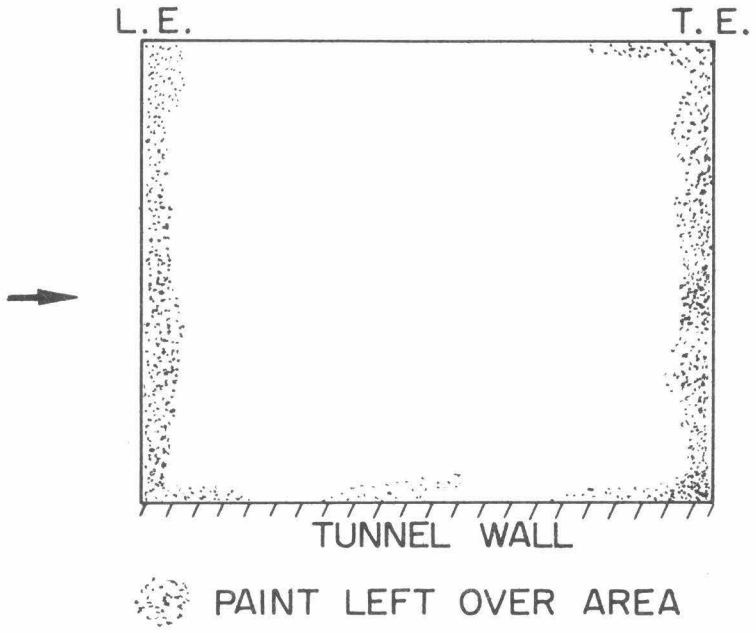

Figure A2.1 Paint pattern left over on the foil surface at zero degree angle of attack and at a velocity of 20 ft/sec.

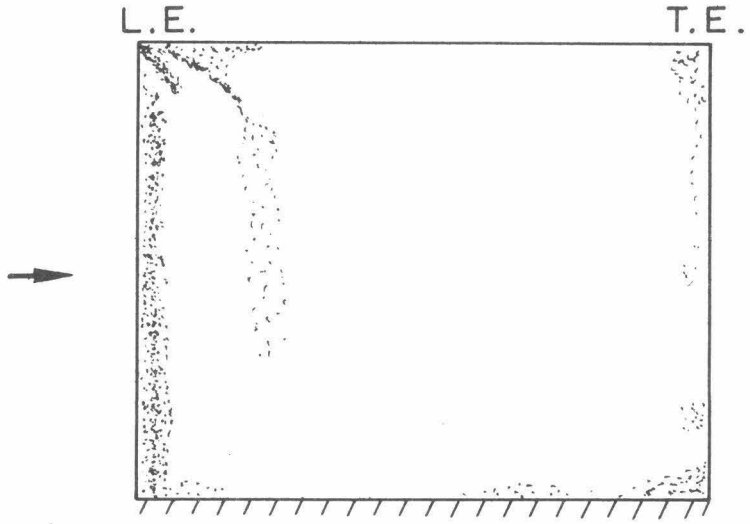

Figure A2.2 Paint pattern left over on the suction side of the foil at 5° angle of attack illustrating a three dimensional flow pattern at a velocity of 20 ft/sec.

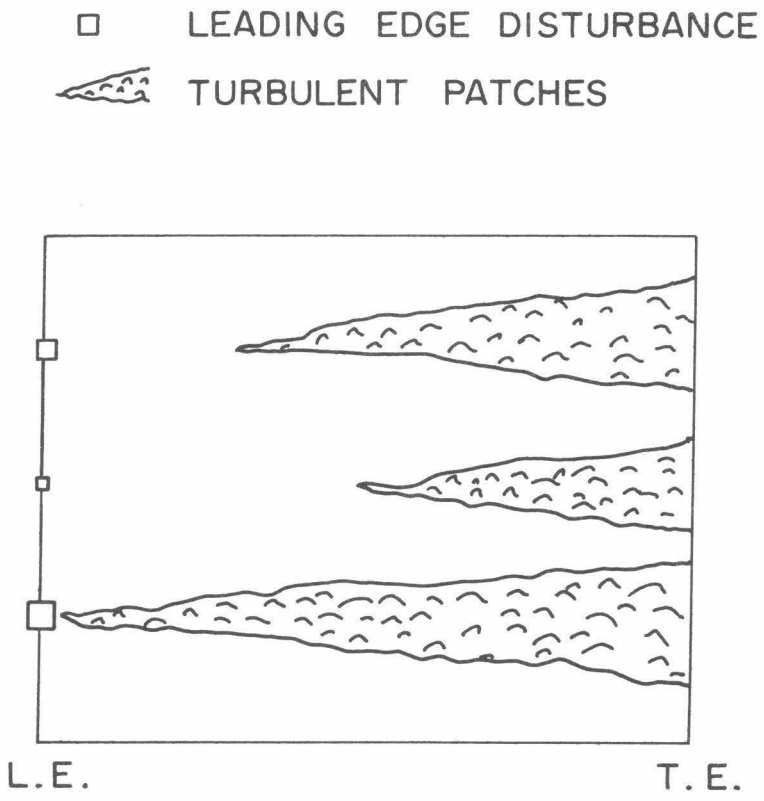

Figure A2.3 Illustration of turbulent patches created by leading edge disturbances.

10 April 1969

DISTRIBUTION LIST FOR UNCLASSIFIED
TECHNICAL REPORTS ISSUED UNDER
CONTRACT Nonr 222(59) TASK 062-010

Technical Library
Building 131
Aberdeen Proving Ground, Maryland 21005

Defense Documentation Center (20)
Cameron Station
Alexandria, Virginia 22314

Technical Library
Naval Ship Research and
Development Center
Annapolis Division
Annapolis, Maryland 21402

Professor Bruce Johnson
Engineering Department
Naval Academy
Annapolis, Maryland 21402

Library
Naval Academy
Annapolis, Maryland 21402

Professor W. P. Graebel
Department of Engineering
Mechanics
The University of Michigan
College of Engineering
Ann Arbor, Michigan 48104

Professor W. R. Debler
Department of Engineering Mechanics
University of Mechanics
Ann Arbor, Michigan 48108

Dr. Francis Ogilvie
Department of Naval Architecture
and Marine Engineering
University of Michigan
Ann Arbor, Michigan 48108

Professor S. D. Sharma
Department of Naval Architecture
and Marine Engineering
University of Michigan
Ann Arbor, Michigan 48108

Professor W. W. Willmarth
Department of Aerospace Engineering
University of Michigan
Ann Arbor, Michigan 48108

Professor Finn C. Michelsen
Naval Architecture and Marine
Engineering
445 West Engineering Bldg.
University of Michigan
Ann Arbor, Michigan 48104

AFOSR (REM)
1400 Wilson Boulevard
Arlington, Virginia 22204

Dr. J. Menkes
Institute for Defense Analyses
400 Army-Navy Drive
Arlington, Virginia 22204

Professor S. Corrsin
Mechanics Department
The Johns Hopkins University
Baltimore, Maryland 20910

Professor O. M. Phillips
The Johns Hopkins University
Baltimore, Maryland 20910

Professor L. S. G. Kovasznay
The Johns Hopkins University
Baltimore, Maryland 20910

Librarian
Department of Naval Architecture
University of California
Berkeley, California 94720

Professor P. Lieber
Department of Mechanical Engineering
University of California
Institute of Engineering Research
Berkeley, California 94720

Professor M. Holt
Division of Aeronautical Sciences
University of California
Berkeley, California 94720

Professor J. V. Wehausen
Department of Naval Architecture
University of California
Berkeley, California 94720

Professor J. R. Paulling
Department of Naval Architecture
University of California
Berkeley, California 94720

Professor E. V. Laitone
Department of Mechanical Engineering
University of California
Berkeley, California 94720

School of Applied Mathematics
Indiana University
Bloomington, Indiana 47401

Commander
Boston Naval Shipyard
Boston, Massachusetts 02129

Director
Office of Naval Research
Branch Office
495 Summer Street
Boston, Massachusetts 02210

Professor M. S. Uberoi
Department of Aeronautical Engineering
University of Colorado
Boulder, Colorado 80303

Naval Applied Science Laboratory
Technical Library
Bldg. 1 Code 222
Flushing and Washington Avenues
Brooklyn, New York 11251

Professor J. J. Foody
Chairman, Engineering Department
State University of New York
Maritime College
Bronx, New York 10465

Dr. Irving C. Statler, Head
Applied Mechanics Department
Cornell Aeronautical Laboratory, Inc.
P. O. Box 235
Buffalo, New York 14221

Dr. Alfred Ritter
Assistant Head, Applied Mechanics Dept.
Cornell Aeronautical Laboratory, Inc.
Buffalo, New York 14221

Professor G. Birkhoff
Department of Mathematics
Harvard University
Cambridge, Massachusetts 02138

Commanding Officer
NROTC Naval Administrative Unit
Massachusetts Institute of Technology
Cambridge, Massachusetts 02139

Professor N. Newman
Department of Naval Architecture and
Marine Engineering
Massachusetts Institute of Technology
Cambridge, Massachusetts 02139

Professor A. H. Shapiro
Department of Mechanical Engineering
Massachusetts Institute of Technology
Cambridge, Massachusetts 02139

Professor C. C. Lin
Department of Mathematics
Massachusetts Institute of Technology
Cambridge, Massachusetts 02139

Professor E. W. Merrill
Department of Mathematics
Massachusetts Institute of Technology
Cambridge, Massachusetts 02139

Professor M. A. Abkowitz
Department of Naval Architecture
and Marine Engineering
Massachusetts Institute of Technology
Cambridge, Massachusetts 02139

Professor G. H. Carrier
Department of Engineering and
Applied Physics
Harvard University
Cambridge, Massachusetts 02139

Professor E. Mollo-Christensen
Room 54-1722
Massachusetts Institute of Technology
Cambridge, Massachusetts 02139

Professor A. T. Ippen
Department of Civil Engineering
Massachusetts Institute of Technology
Cambridge, Massachusetts 02139

Commander
Charleston Naval Shipyard
U. S. Naval Base
Charleston, South Carolina 29408

A. R. Kuhlthau, Director
Research Laboratories for the
Engineering Sciences
Thorton Hall, University of Virginia
Charlottesville, Virginia 22903

Director
Office of Naval Research
Branch Office
219 Dearborn Street
Chicago, Illinois 60604

Library
Naval Weapons Center
China Lake, California 93557

Library MS 60-3
NASA Lewis Research Center
21000 Brookpark Road
Cleveland, Ohio 44135

Professor J. M. Burgers
Institute of Fluid Dynamics and
Applied Mathematics
University of Maryland
College Park, Maryland 20742

Acquisition Director
NASA Scientific & Technical
Information
P. O. Box 33
College Park, Maryland 20740

Professor Pai
Institute for Fluid Dynamics
and Applied Mathematics
University of Maryland
College Park, Maryland 20740

Technical Library
Naval Weapons Laboratory
Dahlgren, Virginia 22448

Computation & Analyses Laboratory
Naval Weapons Laboratory
Dahlgren, Virginia 22448

Professor C. S. Wells
LTV Research Center
Dallas, Texas 75222

Dr. R. H. Kraichnan
Dublin, New Hampshire 03444

Commanding Officer
Army Research Office
Box CM, Duke Station
Durham, North Carolina 27706

Professor A. Charnes
The Technological Institute
Northwestern University
Evanston, Illinois 60201

Dr. Martim H. Bloom
Polytechnic Institute of Brooklyn
Graduate Center, Dept. of Aerospace
Engineering and Applied Mechanics
Farmingdale, New York 11735

Technical Documents Center
Building 315
U. S. Army Mobility Equipment
Research and Development Center
Fort Belvoir, Virginia 22060

Professor J. E. Cermak
College of Engineering
Colorado State University
Ft. Collins, Colorado 80521

Technical Library
Webb Institute of Naval Architecture
Glen Cove, Long Island, New York 11542

Professor E. V. Lewis
Webb Institute of Naval Architecture
Glen Cove, Long Island, New York 11542

Library MS 185
NASA, Langley Research Center
Langley Station
Hampton, Virginia 23365

Dr. B. N. Pridmore Brown
Northrop Corporation
NORAIR-Div.
Hawthorne, California 90250

Dr. J. P. Breslin
Stevens Institute of Technology
Davidson Laboratory
Hoboken, New Jersey 07030

Mr. D. Savitsky
Stevens Institute of Technology
Davidson Laboratory
Hoboken, New Jersey 07030

Mr. C. H. Henry
Stevens Institute of Technology
Davidson Laboratory
Hoboken, New Jersey 07030

Professor J. F. Kennedy, Director
Iowa Institute of Hydraulic Research
State University of Iowa
Iowa City, Iowa 52240

Professor L. Landweber
Iowa Institute of Hydraulic Research
State University of Iowa
Iowa City, Iowa 52240

Professor E. L. Resler
Graduate School of
Aeronautical Engineering
Cornell University
Ithaca, New York 14851

Professor John Miles
% I.G.P.P.
University of California, San Diego
La Jolla, California 92038

Director
Scripps Institution of Oceanography
University of California
La Jolla, California 92037

Dr. B. Sternlicht
Mechanical Technology Incorporated
968 Albany-Shaker Road
Latham, New York 12110

Mr. P. Eisenberg, President
Hydronautics
Pindell School Road
Howard County
Laurel, Maryland 20810 (2)

Professor A. Ellis
University of California, San Diego
Department of Aerospace & Mech. Engrg. Sci.
La Jolla, California 92037

Mr. Alfonso Alcedan L. Director
Laboratorio Nacional De Hydraulics
Antigui Cameno A. Ancon
Casilla Jostal 682
Lima, Peru

Commander
Long Beach Naval Shipyard
Long Beach, California 90802

Professor John Laufer
Department of Aerospace Engineering
University Park
Los Angeles, California 90007

Professor J. Ripkin
St. Anthony Falls Hydraulic Lab.
University of Minnesota
Minneapolis, Minnesota 55414

Professor J. M. Killen
St. Anthony Falls Hydraulic Lab.
University of Minnesota
Minneapolis, Minnesota 55414

Lorenz G. Straub Library
St. Anthony Falls Hydraulic Lab.
Mississippi River at 3rd Avenue SE.
Minneapolis, Minnesota 55414

Dr. E. Silberman
St. Anthony Falls Hydraulic Lab.
University of Minnesota
Minneapolis, Minnesota 55414

Superintendent
Naval Postgraduate School
Library Code 0212
Monterey, California 93940

Professor A. B. Metzner
University of Delaware
Newark, New Jersey 19711

Technical Library
USN Underwater Weapons &
Research & Engineering Station
Newport, Rhode Island 02840

Technical Library
Underwater Sound Laboratory
Fort Trumbull
New London, Connecticut 06321

Professor J. J. Stoker
Institute of Mathematical Sciences
New York University
251 Mercer Street
New York, New York 10003

Engineering Societies Library
345 East 47th Street
New York, New York 10017

Office of Naval Research
New York Area Office
207 W. 24th Street
New York, New York 10011

Director Naval Research Lab
Library Code 2029 (ONRL)
Washington, D.C. 20390

Professor H. Elrod
Department of Mechanical Engineering
Columbia University
New York, New York 10027

Society of Naval Architects and
Marine Engineering
74 Trinity Place
New York, New York 10006

Professor S.A. Piaseck
Department of Engineering Mechanics
University of Notre Dame
Notre Dame, Indiana 46556

Miss O.M. Leach, Librarian
National Research Council
Aeronautical Library
Montreal Road
Ottawa 7, Canada

Technical Library
Naval Ship Research and
Development Center
Panaman City, Florida 32401

Library
Jet Propulsion Laboratory
California Institute of Technology
4800 Oak Grove Avenue
Pasadena, California 91109

Professor M. S. Plesset
Engineering Division
California Institute of Technology
Pasadena, California 91109

Professor H. Liepmann
Department of Aeronautics
California Institute of Technology
Pasadena, California 91109

Technical Library
Naval Undersea R&D Center
3202 E. Foothill Boulevard
Pasadena, California 91107

Professor T. Y. Wu
Department of Engineering
California Institute of Technology
Pasadena, California 91109

Director
Office of Naval Research
Branch Office
1030 E. Green Street
Pasadena, California 91101

Professor A. Acosta
Department of Mechanical Engineering
California Institute of Technology
Pasadena, California 91109

Naval Ship Engineering Center
Philadelphia Division
Technical Library
Philadelphia, Pennsylvania 19112

Technical Library (Code 249B)
Philadelphia Naval Shipyard
Philadelphia, Pennsylvania 19112

Professor R. C. Mac Camy
Department of Mathematics
Carnegie Institute of Technology
Pittsburgh, Pennsylvania 15213

Dr. Paul Kaplan
Oceanics, Inc.
Plainview, Long Island, New York 11803

Technical Library
Naval Missile Center
Point Mugu, California 93441

Technical Library
Naval Civil Engineering Lab.
Port Hueneme, California 93041

Commander
Portsmouth Naval Shipyard
Portsmouth, New Hampshire 03801

Commander
Norfolk Naval Shipyard
Portsmouth, Virginia 23709

Professor F. E. Bisshopp
Division of Engineering
Brown University
Providence, Rhode Island 02912

Dr. L. L. Higgins
TRW Space Technology Labs, Inc.
One Space Park
Redondo Beach, California 90278

Redstone Scientific Information Center
Attn: Chief, Document Section
Army Missile Command
Redstone Arsenal, Alabama 35809

Dr. H. N. Abramson
Southwest Research Institute
8500 Culebra Road
San Antonio, Texas 78228

Editor
Applied Mechanics Review
Southwest Research Institute
8500 Culebra Road
San Antonio, Texas 78206

Librarian
Naval Command Control Communications
Laboratory Center
San Diego, California 92152

Library & Information Services
General Dynamics-Convair
P. O. Box 1128
San Diego, California 92112

Commander (Code 246P)
Pearl Harbor Naval Shipyard
Box 400
FPO San Francisco, California 96610

Technical Library (Code H245C-3)
Hunters Point Division
San Francisco Bay Naval Shipyard
San Francisco, California 94135

Office of Naval Research
San Francisco Area Office
50 Fell Street
San Francisco, California 94103

Dr. A. May
Naval Ordnance Laboratory
White Oak
Silver Spring, Maryland 20910

Fenton Kennedy Document Library
The Johns Hopkins University
Applied Physics Laboratory
8621 Georgia Avenue
Silver Spring, Maryland 20910

Librarian
Naval Ordnance Laboratory
White Oak
Silver Spring, Maryland 20910

Dr. Bryne Perry
Department of Civil Engineering
Stanford University
Stanford, California 94305

Professor Milton Van Dyke
Department of Aeronautical Engineering
Stanford University
Stanford , California 94305

Professor E. Y. Hsu
Department of Civil Engineering
Stanford University
Stanford, California 94305

Dr. R. L. Street
Department of Civil Engineering
Stanford University
Stanford, California 94305

Professor S. Eskinazi
Department of Mechanical Engineering
Syracuse University
Syracuse, New York 13210

Professor R. Pfeffer
Florida State University
Geophysical Fluid Dynamics Institute
Tallahassee, Florida 32306

Professor J. Foa
Department of Aeronautical Engineering
Rennsselaer Polytechnic Institute
Troy, New York 12180

Professor R. C. Di Prima
Department of Mathematics
Rennsselaer Polytechnic Institute
Troy, New York 12180

Dr. M. Sevik
Ordnance Research Laboratory
Pennsylvania State University
University Park, Pennsylvania 16801

Professor J. Lumley
Ordnance Research Laboratory
Pennsylvania State University
University Park, Pennsylvania 16801

Dr. J. M. Robertson
Department of Theoretical and
Applied Mechanics
University of Illinois
Urbana, Illinois 61803

Shipyard Technical Library
Code 130L7 Building 746
San Francisco Bay Naval Shipyard
Vallejo, California 94592

Code L42
Naval Ship Research and
Development Center
Washington, D.C. 20007

Code 800
Naval Ship Research and
Development Center
Washington, D.C. 20007

Code 2027
U. S. Naval Research Laboratory
Washington, D.C. 20390 (6)

Code 438
Chief of Naval Research
Department of the Navy
Washington, D.C. 20360 (3)

Code 513
Naval Ship Research and
Development Center
Washington, D.C. 20007

Science & Technology Division
Library of Congress
Washington, D.C. 20540

ORD 913 (Library)
Naval Ordnance Systems Command
Washington, D.C. 20360

Code 6420
Naval Ship Engineering Center
Concept Design Division
Washington, D.C. 20360

Code 500
Naval Ship Research and
Development Center
Washington, D.C. 20007

Code 901
Naval Ship Research and
Development Center
Washington, D.C. 20007

Code 520
Naval Ship Research and
Development Center
Washington, D.C. 20007

Code 0341
Naval Ship Systems Command
Department of the Navy
Washington, D.C. 20360

Code 2052 (Technical Library)
Naval Ship Systems Command
Department of the Navy
Washington, D.C. 20360

Mr. J. L. Schuler (Code 03412)
Naval Ship Systems Command
Department of the Navy
Washington, D.C. 20360

Dr. J. H. Huth (Code 031)
Naval Ship Systems Command
Department of the Navy
Washington, D.C. 20360

Code 461
Chief of Naval Research
Department of the Navy
Washington, DC. 20360

Code 530
Naval Ship Research and
Development Center
Washington, D.C. 20360

Code 466
Chief of Naval Research
Department of the Navy
Washington, D.C. 20360

Office of Research and Development
Maritime Administration
441 G. Street, NW.
Washington, D.C. 20235

Code 463
Chief of Naval Research
Department of the Navy
Washington, D.C. 20360

National Science Foundation
Engineering Division
1800 G. Street, NW.
Washington, D.C. 20550

Dr. G. Kulin
National Bureau of Standards
Washington, D.C. 20234

Department of the Army
Coastal Engineering Research Center
5201 Little Falls Road, NW.
Washington, D.C. 20011

Code 521
Naval Ship Research and
Development Center
Washington, D.C. 20007

Code 481
Chief of Naval Research
Department of the Navy
Washington, D.C. 20390

Code 421
Chief of Naval Research
Department of the Navy
Washington, D.C. 20360

Commander
Naval Ordnance Systems Command
Code ORD 035
Washington, D.C. 20360

Librarian Station 5-2
Coast Guard Headquarters
1300 E. Street, NW.
Washington, D.C. 20226

Division of Ship Design
Maritime Administration
441 G. Street, NW.
Washington, D.C. 20235

HQ USAF (AFRSTD)
Room 1D 377
The Pentagon
Washington, D.C. 20330

Commander
Naval Ship Systems Command
Code 6644C
Washington, D.C. 20360

Dr. A. Powell (Code 01)
Naval Ship Research and
Development Center
Washington, D.C. 20007

Director of Research Code RR
National Aeronautics & Space Admin.
600 Independence Avenue, SW.
Washington, D.C. 20546

Commander
Naval Ordnance Systems Command
Code 03
Washington, D.C. 20360

Code ORD 05411
Naval Ordnance Systems Command
Washington, D.C. 20360

m AIR 5301
Naval Air Systems Command
Department of the Navy
Washington, D.C. 20360

AIR 604
Naval Air Systems Command
Department of the Navy
Washington, D.C. 20360

Dr. John Craven (PM 1100)
Deep Submergence Systems
Project
Department of the Navy
Washington, D.C. 20360

Code 522
Naval Ship Research and
Development Center
Washington, D.C. 20007

Commander
Naval Oceanographic Office
Washington, D.C. 20390

Chief of Research & Development
Office of Chief of Staff
Department of the Army
The Pentagon, Washington, D.C. 20310

Code 6342A
Naval Ship Systems Commmand
Department of the Navy
Washington, D.C. 20360

Code 468
Chief of Naval Research
Department of the Navy
Washington, D.C. 20360

Director
U. S. Naval Research Laboratory
Code 6170
Washington, D.C. 20390

Code 473
Chief of Naval Research
Department of the Navy
Washington, D.C. 20360

Code 6100
Naval Ship Engineering Center
Department of the Navy
Washington, D.C. 20360

Mr. Ralph Lacey (Code 6114)
Naval Ship Engineering Center
Department of the Navy
Washington, D.C. 20360

Dr. A. S. Iberall, President
General Technical Services, Inc.
451 Penn Street
Yeadon, Pennsylvania 19050

Dr. H. Cohen
IBM Research Center
P. O. Box 218
Yorktown Heights, New York 10598

Unclassified
Security Classification

DOCUMENT CONTROL DATA - R & D

(Security classification of title, body of abstract and indexing annotation must be entered when the overall report is classified)

1. ORIGINATING ACTIVITY *(Corporate author)*

Hydrodynamics Laboratory
California Institute of Technology
Pasadena, California

2a. REPORT SECURITY CLASSIFICATION

Unclassified

2b. GROUP

3. REPORT TITLE

Water Tunnel Investigations of Scale Effects in Cavitation Detachment from Smooth Slender Bodies and Characteristics of Flow Past a Bi-Convex Hydrofoil

4. DESCRIPTIVE NOTES *(Type of report and inclusive dates)*

5. AUTHOR(S) *(First name, middle initial, last name)*

Vijay H. Arakeri

6. REPORT DATE	7a. TOTAL NO. OF PAGES	7b. NO. OF REFS
January, 1971	82	16

8a. CONTRACT OR GRANT NO.	9a. ORIGINATOR'S REPORT NUMBER(S)
Nonr 220(59)	
b. PROJECT NO.	E-79A.12
c.	9b. OTHER REPORT NO(S) *(Any other numbers that may be assigned this report)*
d.	

10. DISTRIBUTION STATEMENT

11. SUPPLEMENTARY NOTES	12. SPONSORING MILITARY ACTIVITY
	Office of Naval Research Department of the Navy

13. ABSTRACT

Experimental results concerning force coefficients and cavity detachment points under various cavitating conditions on two geometrically similar bi-convex hydrofoils are presented. A linearized cavity flow theory with cavitation separation points determined from the assumption of smooth separation at the detachment point is presented and a comparison is made of these theoretical results with the experiments. Scaling problems with cavitation separation from smooth slender bodies are discussed. With the help of photographic studies three different types of cavitation separation from smooth bodies are proposed.

DD FORM 1 NOV 65 1473 (PAGE 1)

S/N 0101-807-6801

Unclassified
Security Classification

14. KEY WORDS	LINK A		LINK B		LINK C	
	ROLE	WT	ROLE	WT	ROLE	WT
Cavitation						
Smooth Detachment						
Scale Effects						
Biconvex-hydrofoil						